

Dear Reviewers,

we really appreciate the time you have taken to explain your intuition and concerns. In these times of covid-19 induced isolation due to cancelled workshops and conferences (such as URSI GA to name one), discussions of ones work and ideas are hard to come by. As exemplified further below, discussion is really important to improve ones work!

We believe to now have fully understood the situation and that there have been two parallel misunderstandings. First of all, the intuition from Reviewer #2 that the inner product is a better indicator for ambiguities than the distance was correct. However, the reason behind the intuition was initially not communicated or maybe not conceptualized enough for us to understand it. The constant phase offset on one element that was discussed is indeed a property of the function $|\langle \mathbf{x}, \mathbf{y} \rangle|$ and not of $|\mathbf{x} - \mathbf{y}|$. The confusion on our side arose since it is not directly this property that makes the inner product a better indicator. It was also unfortunate that in all the specific cases that we had manually validated, this distinction did not matter.

We had considered previously the practical difference between $f(\mathbf{y}) = |\langle \mathbf{x}, \mathbf{y} \rangle|$ versus $f(\mathbf{y}) = \langle \mathbf{x}, \mathbf{y} \rangle$, i.e. that the first possesses less unique information since it does not preserve the relative orientation of \mathbf{y} . I.e. if \mathbf{y} is at the same angle from \mathbf{x} , but directed "towards" \mathbf{x} or "away from" \mathbf{x} , it gives the same value for $f(\mathbf{y})$, but gives very different values when using $\langle \mathbf{x}, \mathbf{y} \rangle$. The distance between two points preserve the relative orientation. This leads us to our second miss-understanding. We had erroneously assumed MUSIC preserves the relative orientation, when indeed it does not. MUSIC is the norm of a projection onto the complement space of the signal subspace, which means that the projection does not have a sense of orientation towards the signal subspace basis vector.

We can now see how the invariance to projection orientation can directly translate to an invariance of a constant phase offset on one of the vectors in the inner product, just like Reviewer #2 stated. In complex vector spaces, the base space is the complex plane \mathbb{C} . This means that "projection orientation" is two-dimensional instead of one-dimensional as with real spaces. So, if the projection is a complex number $a = \langle \mathbf{x}, \mathbf{y} \rangle$, any rotation of this number $ae^{i\theta}$ should not affect the result. This can be re-written as $\langle \mathbf{x}, \mathbf{y}e^{i\theta} \rangle$.

To remedy our misunderstandings, we have recalculated every single result in the paper with the new absolute value inner product definition instead of the original distance function. We have rewritten the ambiguity definition part (and as a consequence revised the rest of the manuscript to contain the updated definition), adding also the above discussion, and finally updated the appendices to use the inner product definition (without any need to change their results). We have scrutinized all recalculated results and plots and updated the text in the results section accordingly.

To summarize: there were no large practically important changes in the results. This was expected as nothing changed about the used DOA determination but only the discretization. In terms of the discretization, we have not fine-tuned the limiting values for including ambiguities and second-order ambiguities to match the previous number of ambiguities considered. Therefore, the number of visualised discretized input/output (and their numbering) have changed in many of the simulations. However, these newly considered locations were unused in almost all situations (P matrix element ≈ 0 at every SNR) except some cases for the MU and MAARSY radar subgroup models where the input DOA was in an close to undeterminable region (dark color region in Figure 6) and the new discretization had an impact. Comparing old Figure 14, input 2, with new Figure 14, input 8, a previously unconsidered ambiguity now has high probability instead of algorithm failure. The limiting SNR for unambiguous determination is still unchanged, but the onset of algorithm failure is sometimes changed. The onset difference varies from most commonly zero dB to the worst case given in Input 2, Figure 14, where it changed by 20–30 dB.

The difference in discretization can also be seen in Figure 8. But even though this figure looks quantitatively different then previously, qualitatively the dynamics of the resulting P-matrix (Figure 11–12) as a function of SNR is mostly the same. Inputs 5–6 in Figure 9 differ from the previous version, since the old

Figure 9 was calculated without using the scattered gradient ascent version of MUSIC, while this time the updated implementation was used. Additionally, for these two input locations a new ambiguity previously not considered was introduced. The other Inputs are unchanged.

We discovered that a quick way to manually scrutinize the Monte-Carlo data is to animate the DOA Determination as a function of SNR. We have now included such an animation in the data repository (the data upload has not been approved by SND yet, upon request we can send a direct link to the animation).

We will give the manuscript to the Copernicus English copy-editing services to improve grammatical accuracy and overall readability before publication.

Probabilistic analysis of ambiguities in radar echo direction of arrival from meteors

Daniel Kastinen^{1,2} and Johan Kero¹

¹Swedish Institute of Space Physics (IRF), Box 812, SE-98128 Kiruna, Sweden

²Umeå University, Department of Physics, SE-90187 Umeå, Sweden

Correspondence: Daniel Kastinen (daniel.kastinen@irf.se)

Abstract. Meteors and hard targets produce coherent radar echoes. If measured with an interferometric radar system, these echoes can be used to determine the position of the target through finding the Direction Of Arrival (DOA) of the incoming echo onto the radar. Depending on the spatial configuration of radar receiving antennas and their individual gain patterns, there may be an ambiguity problem when determining the DOA of an echo. Radars that are theoretically ambiguity free are known to still have ambiguities that depend on the total radar Signal to Noise Ratio (SNR). In this study we investigate robust methods which are easy to implement to determine the effect of ambiguities on any hard target DOA determination by interferometric radar systems. We apply these methods specifically to simulate four different radar systems measuring meteor head and trail echoes using the multiple signal classification (MUSIC) DOA determination algorithm. The four radar systems are the middle and upper atmosphere (MU) radar in Japan, a generic Jones 2.5λ specular meteor trail radar configuration, the Middle Atmosphere Alomar Radar System (MAARSY) radar in Norway and the Program of the Antarctic Syowa Mesosphere Stratosphere Troposphere Incoherent Scatter (PANSY) radar in the Antarctic. We also examined a slightly perturbed Jones 2.5λ configuration used as a meteor trail echo receiver for the PANSY radar. All the results are derived from simulations and their purpose is to grant understanding of the behaviour of DOA determination. General results are: there may be a region of SNRs where ambiguities are relevant; Monte Carlo simulation determines this region and if it exists; the MUSIC function peak value is directly correlated with the ambiguous region; a Bayesian method is presented that may be able to analyse echoes from this region; the DOA of echoes with SNRs larger than this region are perfectly determined; the DOA of echoes with SNRs smaller than this region completely fail to be determined; the location of this region is shifted based on the total SNR versus the channel SNR in the direction of the target; asymmetric subgroups can cause ambiguities even for "ambiguity free" radars. For a DOA located at the zenith, the end of the ambiguous region is located at 17 dB SNR for the MU radar and 3 dB SNR for the PANSY radar. The Jones radars are usually used to measure specular trail echoes far from zenith. The ambiguous region for a DOA at 75.5° elevation and 0° azimuth ends at 12 dB SNR. Using the Bayesian method it may be possible to analyse echoes down to 4 dB SNR for the Jones configuration, given enough data points from the same target. The PANSY meteor trail echo receiver did not deviate significantly from the generic Jones configuration. The MAARSY radar could not resolve arbitrary DOAs sufficiently well to determine a stable region. However, if the DOA search is restricted to 70° elevation or above by assumption, stable DOA determination occurs above 15 dB SNR.

1 Introduction

Radar systems are a vital part of current research infrastructure. They are used for a wide variety of novel, (e.g. Sato et al., 2014; Kero et al., 2012b; McCrea et al., 2015), and routine remote sensing observations (e.g. Hocking, 2005, and references
30 therein). One subset of these observations are objects and phenomena in the atmosphere that produce coherent radar echoes. Meteor head and trail echoes, satellite and space debris echoes, polar mesospheric echoes, field aligned irregularities and many more phenomena fall under this category. However, to discern the position and motion of these radar targets, interferometric or multi-static radar systems must be used.

When determining the position of an object by interferometry, there is an ambiguity problem (Schmidt, 1986). The position
35 is determined by finding the Direction Of Arrival (DOA) of the incoming echo onto the radar. Depending on the spatial configuration of the receiving antennas and their individual gain patterns, the voltage response can be the same for several different plane wave DOA's, thereby making it impossible to determine the correct direction. This problem is general to all DOA determinations made by radar systems with interferometry base lines longer than half a wavelength. In this study it is put in the context of meteor head- and trail echo observations.

40 Every day the Earth's atmosphere is bombarded by billions of dust-sized particles and larger pieces of material from space. This incoming material gives us a unique opportunity to examine the motion and population of small bodies in the solar system (e.g. Vaubaillon et al., 2005a, b; Kastinen and Kero, 2017). Objects with sizes between 100 microns and 1 metre moving in interplanetary space are called meteoroids. Meteoroids originate from comets and asteroids, they are abundant and can have high velocities (Whipple, 1951). When meteoroids enter the atmosphere they burn up causing a phenomenon called a meteor
45 (Ceplecha et al., 1998). The meteor itself can be divided into two parts that function as hard targets: the dense plasma co-moving with the ablating meteoroid and the trail of diffusing plasma left in the atmosphere. These generate the meteor head and trail echoes.

Meteor trail plasma drifts with the ambient atmosphere. The drift velocity is therefore a measure of the neutral wind at the observation altitude. The typical ablation altitude where meteor phenomena occur lie between 70 and 130 km. This region is
50 characterized by variability driven by atmospheric tides as well as planetary and smaller scale gravity waves. Specular meteor trail radars have become widespread scientific instruments to study atmospheric dynamics deployed at locations covering latitudes from Antarctica to the Arctic Svalbard (Kero et al., 2019). To calculate the neutral wind, the DOA of the specular echo must be determined.

Due to the altitude distribution of meteor phenomena, the far field approximation is almost always valid, which means that
55 an incoming echo can be modeled as a plane wave (Kildal, 2015). The only exception is the Arecibo radio telescope due to its 300 m diameter large spherical reflector at a 430 MHz operating frequency. Using an interferometric radar system to determine the DOA of a meteor head echo as a function of time allows the construction of a meteoroid trajectory (e.g. Kero et al., 2012b; Jones et al., 2005, 1998; Szasz et al., 2008; Chau and Woodman, 2004; Close et al., 2000). This trajectory is the base for

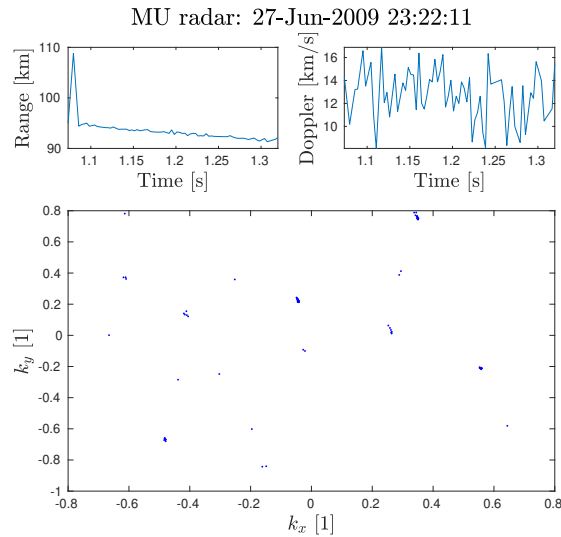


Figure 1. Example meteor head event measured with the MU radar which seem ambiguous. The upper left panel is the one way range, the upper right panel is the line of sight velocity, and the bottom panel is the normalized wave vector ground projection. The wave vector $+y$ -axis is aligned with North and the $+x$ -axis with the East. The SNR varied between 8-16 dB for this event. The goal of this paper is to understand enough about DOA determination behaviour to investigate these types of events.

60 computing the meteor position and meteoroid velocity, radar cross section, and for reconstructing the original meteoroid solar system orbit.

There are analytic methods to determine all the ambiguities present in a radar system, although these scale poorly and have several restrictions (Kastinen, 2018; Schmidt, 1986). Systems that have no theoretical ambiguities also suffer from ambiguous DOA solutions due to noise (Kastinen, 2018; Jones et al., 1998). These so-called noise-induced ambiguities are not multiple solutions to the DOA determination. Instead, the DOA determination output becomes a stochastic variable that is no longer centered on the true DOA but is spread out between several different DOA solutions with similar radar responses. Thus, when determining the DOA of a noisy signal there is a probability of miss-classifying the DOA. This miss-classification probability is separate from the DOA error introduced by the noise that is usually the focus in measurement pipelines (Kero et al., 2012b) and depends on the Signal to Noise Ratio (SNR) of the received signal. In these cases Point Spread Functions (PSFs) have been used to determine the morphology of expected ambiguities. However, these do not relate SNR to DOA miss-classification probabilities (Chau and Clahsen, 2019). The morphology of the PSF may also depend on the input DOA itself (further discussed in Appendix B).

75 The existence of head echo events such as the one illustrated in Fig. 1 is the reason that prompted this study. This meteor is seemingly jumping from place to place in the sky even though the range and line of sight velocity was well determined. This was a special case among thousands of other successful and validated measurements using the same analysis and system. Hence, the goal of this study is to understand enough about DOA determination behaviour to investigate these types of events,

especially today when analysis is automated and databases can contain millions of events (Campbell-Brown, 2019). If even a small fraction of these events stand out as interesting but are the result of ambiguities or other artifacts, consequent research can be negatively influenced. On the other hand, given strange results, large portions of data may be discarded when in fact some are not a consequence of ambiguities or algorithmic errors (Schult et al., 2013). Having a good understanding of DOA
80 determination behaviour may also allow us to analyse events with lower SNR than currently (Jones et al., 1998).

There are no methods, to our knowledge, to resolve noise-induced ambiguities in DOA determinations or to determine the probability of miss-classification. We have therefore extended upon the study performed in Kastinen (2018).

In Sect. 2 we present a numerical method for determining the DOA ambiguities, which works irrespective of whether the ambiguities are noise-induced or not. The method can be applied on arbitrary radar systems and experience no large scaling
85 problems with system complexity. It also allows for arbitrary receiver models to be used.

Section 3 provides an overview of how we have applied the multiple signal classification (MUSIC) algorithm. The MUSIC method allows for an arbitrary sensor response model and can thus be applied on any radar system.

We have focused on radars measuring the meteor phenomena. However, the analysis methods applied are usable on any kind of interferometric hard-target detections made by radars. The radars that we have applied these techniques on are described in
90 Sect. 4 and the results are presented in Sect. 5. The results for each system is also discussed in its respective subsection. Finally we conclude the results and discuss the overall results in Sect. 6.

2 Method

2.1 Ambiguities

To find the ambiguities present when determining the DOA, we need a radar sensor response model Φ . A model for a radar with
95 antennas at locations \mathbf{r}_j , with individual complex gain functions $g_j(\mathbf{k})$, receiving a plane wave of amplitude A is described by

$$\Phi(\mathbf{k}) = \begin{pmatrix} Ag_1(\mathbf{k})e^{-i\langle \mathbf{k}, \mathbf{r}_1 \rangle_{\mathbb{R}^3}} \\ \vdots \\ Ag_N(\mathbf{k})e^{-i\langle \mathbf{k}, \mathbf{r}_N \rangle_{\mathbb{R}^3}} \end{pmatrix}. \quad (1)$$

Here \mathbf{k} is the wave-vector of the incoming plane wave. We denote the inner product of a space X by $\langle \cdot, \cdot \rangle_X$, i.e. $\langle \cdot, \cdot \rangle_{\mathbb{R}^3}$ is the real 3-dimensional inner product. In the case of radar systems with sub-arrays, the $g_j(\mathbf{k})$ functions can be defined as

$$g_j(\mathbf{k}) = \sum_{l=1}^{N_j} \gamma_{jl}(\mathbf{k})e^{-i\langle \mathbf{k}, \mathbf{r}_j - \boldsymbol{\rho}_{jl} \rangle_{\mathbb{R}^3}}, \quad (2)$$

100 where $\gamma_{jl}(\mathbf{k})$ are the antennas' individual gain functions and $\boldsymbol{\rho}_{jl}$ are the sub-array antenna locations. In this case the \mathbf{r}_j locations are the geometric centers of the sub-arrays, i.e. the phase centers. In all radar systems we consider, the same type of antennas are used throughout the system. Also, we are not aware of any studies that find variability in individual antenna gain patterns due to effects like mutual coupling for the radar systems we have investigated. As such, we can use a common function for all antennas $\gamma_{jl}(\mathbf{k}) = \gamma(\mathbf{k})$.

105 Usually, the wave amplitude A is unknown and the DOA determination algorithm should therefore be invariant of signal amplitude $|\Phi(\mathbf{k})|$. As such, our definition of an ambiguity should also be invariant of signal amplitude.

In the pursuit of an analytical solution, Kastinen (2018) was unable to include the variable gain patterns g_i of the radar channels in the formula for finding ambiguities. The calculation method presented there scaled badly with the number of channels in the system and was not invariant to signal amplitude. We have resolved these issues, thereby allowing for any model Φ to be used, by numerically finding ambiguities on a case by case basis.

The normalized sensor response model is written as

$$\frac{\Phi(\mathbf{k})}{|\Phi(\mathbf{k})|} = \hat{\Phi}(\mathbf{k}). \quad (3)$$

Ambiguities are formed when

$$\frac{\Phi(\mathbf{k}_0)}{|\Phi(\mathbf{k}_0)|} \left| \left\langle \hat{\Phi}(\mathbf{k}_0), \hat{\Phi}(\mathbf{k}) \right\rangle_{\mathbb{C}^N} \right| \approx \frac{\Phi(\mathbf{k})}{|\Phi(\mathbf{k})|} \mathbb{1} : \mathbf{k}_0 \not\approx \mathbf{k}. \quad (4)$$

115 Exactly what the conditions "approximate to" and "not approximate to" mean in this definition needs to be decided on a case by case basis as explained further below. The ~~normalized sensor response model is written as~~

$$\frac{\Phi(\mathbf{k})}{|\Phi(\mathbf{k})|} = \hat{\Phi}(\mathbf{k}).$$

reason for this specific definition will also be covered further below. Equation 4 is invariant to the individual antenna gain $\gamma(\mathbf{k})$.

Thus, we may define $\gamma(\mathbf{k}) = 1$ for all examined radar systems.

120 We call an ambiguity perfect, i.e. unambiguous DOA determination is impossible even at infinite SNR, if ~~$\hat{\Phi}(\mathbf{k}_0) = \hat{\Phi}(\mathbf{k}) : \mathbf{k}_0 \neq \mathbf{k}$~~ $\left| \left\langle \hat{\Phi}(\mathbf{k}_0), \hat{\Phi}(\mathbf{k}) \right\rangle_{\mathbb{C}^N} \right| \approx 1$.

We define a set of ambiguities to \mathbf{k}_0 as the vectors \mathbf{k} that fulfill Eq. 4, i.e.

$$\Omega(\mathbf{k}_0) = \{ \mathbf{k} : \left| \left\langle \hat{\Phi}(\mathbf{k}_0), \hat{\Phi}(\mathbf{k}) \right\rangle_{\mathbb{C}^N} \right| \approx 1 : \mathbf{k}_0 \not\approx \mathbf{k} \}. \quad (5)$$

It is important to note that it is not sufficient to calculate the set of ambiguities for only one \mathbf{k}_0 , as this set may not display the same pattern as the set for another direction \mathbf{k}_1 .

125 Following the definition in Eq. 4, an indicator function of ambiguities is the normalized sensor response ~~distance-inner~~ product

$$d(\mathbf{k}) = \left| \left\langle \hat{\Phi}(\mathbf{k}_0), \hat{\Phi}(\mathbf{k}) \right\rangle_{\mathbb{C}^N} \right|. \quad (6)$$

There are several other ways to define ambiguities. The requirement is that the definition is invariant of sensor response norm and to a constant phase offset in all dimensions. ~~One of the~~ Which definition to use depend on the behaviour of the DOA determination algorithm. One important property of algorithms is whether or not they preserve orientation with respect to $\hat{\Phi}(\mathbf{k}_0)$. Neither the MUSIC algorithm (cf. Sect. 3) nor Equation 6 preserve orientation. The latter is visualized by imagining the inner product as a scalar projection of $\hat{\Phi}(\mathbf{k})$ onto $\hat{\Phi}(\mathbf{k}_0)$. This projection contains the orientation of $\hat{\Phi}(\mathbf{k})$ with respect to

$\hat{\Phi}(\mathbf{k}_0)$. For real vector spaces, the orientation is expressed in terms of + or -, while for complex vector spaces in the form of the phase of the complex number. The orientation is disregarded in Eq. 6 when we apply the absolute value.

135 One of several possible other formulations is using ~~the inner product~~ a distance function. The definition would then be $d(\mathbf{k}) = \frac{\langle \hat{\Phi}(\mathbf{k}_0), \hat{\Phi}(\mathbf{k}) \rangle_{\mathbb{C}^N}}{\|\hat{\Phi}(\mathbf{k}_0)\| \|\hat{\Phi}(\mathbf{k})\|}$. This equation ~~$d(\mathbf{k}) = \|\hat{\Phi}(\mathbf{k}_0) - \hat{\Phi}(\mathbf{k})\|$~~ . This is not invariant to the orientation. One can also create a function that is not invariant using the inner product defined in Eq. 6 but not applying the absolute value, i.e. $d(\mathbf{k}) = \langle \hat{\Phi}(\mathbf{k}_0), \hat{\Phi}(\mathbf{k}) \rangle_{\mathbb{C}^N}$. These equations and Eq. 6 ~~would produce equivalent solutions~~ often produce equivalent solution sets given an ambiguity search. ~~The only difference is that when using the inner product, the search would maximize rather than minimize the function. Both definitions produce the same qualitative information, but quantitatively different, but not always, depending on search algorithm configurations.~~ We have elected to use Eq. 4 to define an ambiguity as it is more straightforward due to its literal translation: "the normalized sensor response of \mathbf{k}_0 is approximately equal to the normalized sensor response of \mathbf{k} where \mathbf{k}_0 is not close to \mathbf{k} " ~~6~~ as an ambiguity indicator function since it well describes the behaviour of MUSIC.

145 If the set $\Omega(\mathbf{k}_0)$ is finite, the ~~distance indicator~~ function d must have ~~valleys peaks~~ with a single point ~~bottom top~~ at every \mathbf{k} in $\Omega(\mathbf{k}_0)$. These ~~valleys peaks~~ \mathbf{k} are separated from \mathbf{k}_0 and have ~~a depth heights~~ d that are used to decide if they ~~are should be~~ included in the ambiguity set $\Omega(\mathbf{k}_0)$ or not. As the ~~valleys peaks~~ identify ambiguities, we have implemented a scattered gradient ~~deseent ascent~~ method to determine the ambiguity set Ω for a given \mathbf{k}_0 . The ~~step-by-step step-by-step~~ method is as follows:

1. Define a source wave direction \mathbf{k}_0 .
- 150 2. Generate a set of n start wave vectors $\{\mathbf{a}_i\}$ distributed (e.g. uniformly) on the hemisphere.
3. For each start wave vector \mathbf{a}_i , do a gradient ~~deseent ascent~~ search using the gradient of Eq. 6, $\nabla d(\mathbf{k})$.
4. Collect the ~~valley peak~~ locations $\{\mathbf{b}_i\}$ and ~~valley depths peak heights~~ $\{d(\mathbf{b}_i)\}$
5. Remove duplicate results yielding the set of all ambiguities and their ~~depths peaks~~ $\{\mathbf{k}_i, d(\mathbf{k}_i)\}$.

This method can be used with any sensor response, d model to find ambiguities. After the set $\{\mathbf{k}_i, d(\mathbf{k}_i)\}$ is acquired, it is necessary to filter the set based on what is deemed approximate and not approximate as per Eq. 5. This is done based on ~~some maximum valley depth~~ a maximum peak height ϵ_d and ~~some a~~ minimum separation from \mathbf{k}_0 . The filtering prevents the inclusion of ambiguities that only appear at unrealistically low SNR's. We will from here on denote this filtered set of ambiguities by $\Omega(\mathbf{k}_0) = \{\mathbf{k}_i\}$.

An important factor to note is that these ambiguities are **not** necessarily transitive relations. They are only transitive when 160 the ~~distance is 0~~ indicator function is 1, i.e. they occupy the same point in sensor response space. The non-transitive relationship means that for ~~$d > 0$~~ $d < 1$, if \mathbf{k}_1 is ambiguous with \mathbf{k}_2 and \mathbf{k}_2 is ambiguous with \mathbf{k}_3 , \mathbf{k}_1 does not have to be ambiguous with \mathbf{k}_3 .

2.2 Noise

All the radar systems considered in this study have operating frequencies in the Very High Frequency (30–300 MHz) range. In this range, the galactic background radiation dominates the noise (e.g. Bianchi and Meloni, 2007). This noise can be well modeled (e.g. Polinsky, 2007). When measured by an antenna, the noise is modeled as a circularly-symmetric complex normal random variable. Such a distribution is defined as $\mathcal{CN}(\boldsymbol{\mu} = \mathbf{0}, \Sigma, C = 0)$ where $\boldsymbol{\mu}$ is the complex mean vector, Σ is the covariance matrix and C is the relation matrix. We assume that the noise dynamics is the same for every channel of a N channel radar system. We can thus use N random variables in a one-dimensional complex space instead of an N dimensional complex space. Furthermore, since the distribution is circularly-symmetric we define the controlling variable to be the variance of a single component, i.e. the real or imaginary variance σ_c^2 . The covariance matrix then becomes $\Sigma = 2\sigma_c^2$. The sensor noise is defined as

$$\boldsymbol{\xi} = \begin{pmatrix} \xi_1 \\ \vdots \\ \xi_N \end{pmatrix}, \quad (7)$$

$$\xi_i \sim \mathcal{CN}(0, 2\sigma_c^2, 0). \quad (8)$$

In pseudo code the noise can now be simulated as `xi = (rand_normal(N) + li*rand_normal(N))*sigma_c`.

2.3 Signal to Noise ratio

In order to relate results from simulations to measured data, the noise-controlling variable σ_c needs to be related to a measured SNR. We have chosen to use an SNR that is calculated after coherently integrating over all radar channels. The noisy signal power is then defined as

$$P = \left| \sum_{i=1}^N \Phi_i + \xi_i \right|^2. \quad (9)$$

When we propagate the stochastic variables using standard properties of complex normal distributions we find that

$$N\sigma_c^2 P \sim \chi^2(\lambda, 2), \quad (10)$$

where $\chi^2(\lambda, 2)$ is the non-central chi-squared distribution of order 2 with λ parameter

$$\lambda = \frac{1}{N} \left(\frac{AG(\mathbf{k})}{\sigma_c} \right)^2. \quad (11)$$

The order of a non-central chi-squared distribution is equal to the number of squared normal distributions that are summed, while the lambda parameter is related to their mean values. Here A is the signal amplitude and $G(\mathbf{k})$ describes the one-directional gain in the source direction, i.e

$$G(\mathbf{k}) = \left| \sum_{i=1}^N \frac{1}{A} \Phi_i(\mathbf{k}) \right|. \quad (12)$$

The expected value of the power is then

$$190 \quad \mathbb{E}[P] = (AG(\mathbf{k}))^2 + 2N\sigma_c^2. \quad (13)$$

Setting $A = 0$ gives the noise power $\mathbb{E}[P_n] = 2N\sigma_c^2$ and setting $\sigma_c = 0$ gives the signal power $\mathbb{E}[P_s] = (AG(\mathbf{k}))^2$. SNR is defined as the ratio between the signal power and the noise power, i.e.

$$\text{SNR} = \frac{\mathbb{E}[P_s]}{\mathbb{E}[P_n]} = \frac{\mathbb{E}[P]}{\mathbb{E}[P_n]} - 1 = \frac{1}{2N} \left(\frac{AG(\mathbf{k})}{\sigma_c} \right)^2. \quad (14)$$

Assuming we have two measurements, one of the noise power $\mathbb{E}[P_n]$ and one of the noisy signal power $\mathbb{E}[P]$, an SNR that is
 215 equivalent to that used in our simulations can be calculated for any detected signal. Using Eq. 14, an appropriate σ_c for a given SNR can be chosen for a simulation.

2.4 Direct Monte Carlo

Given a sensor response model and a noise model we can perform a direct Monte Carlo (MC) on any DOA determination algorithm. Given a true direction \mathbf{k}_i , the theoretical noisy sensor response model is $\Phi(\mathbf{k}_i) + \xi$. Then, a DOA determination
 200 algorithm F can find an estimation of the source direction as,

$$F(\Phi(\mathbf{k}_i) + \xi) = \tilde{\mathbf{k}}. \quad (15)$$

Thus, the estimated source direction $\tilde{\mathbf{k}}$ also becomes a distribution. We can sample this DOA determination output distribution by sampling the noisy signal distribution $\Phi(\mathbf{k}_i) + \xi$ and applying the DOA determination algorithm F on each sample. An example MC sampling of such a DOA output distribution is illustrated in Fig. 2. This example was generated using the generic
 205 Jones 2.5λ sensor response model further described in Sect. 4.1. This radar model does not contain any perfect ambiguities, yet at this SNR the DOA output is stochastically clustered around noise-induced ambiguities. The DOA determination was made using the multiple signal classification (MUSIC) algorithm described in Sect. 3. The interesting aspect that will allow qualitative evaluation of measurement data is how the DOA output behaviour evolves as a function of SNR, true DOA, sensor response model, and DOA determination algorithm. In Sect 5 we examine the first three of these components while keeping
 210 the DOA determination algorithm fixed.

2.5 Discretising the problem

The example MC DOA determination simulation in Fig. 2 contain apparent noise-induced ambiguities alongside the spread of the DOA estimation around the input direction and its ambiguities. This sampling of $\tilde{\mathbf{k}}$ represents a continuous distribution that contains information about both the DOA determination accuracy and possible ambiguities. There are many works that
 215 describe the error distribution of MUSIC for DOA determination in radars (e.g. Kangas et al., 1994, 1996; Ferreol et al., 2006). [However Here](#), we focus on the probability of ambiguous DOA output and general algorithm stability. Therefore we discretise the problem by using the set of known ambiguities $\mathbf{k}_i \in \Omega(\mathbf{k}_0)$ described in Sect. 2.1.

2.5 Lambda radar: MC DOA determination, 10.69 dB SNR

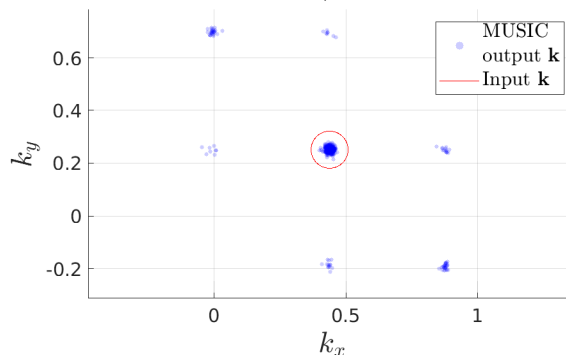


Figure 2. Example MC DOA determination simulation with 500 samples. The generic Jones 2.5λ radar model as described by Eq. 30 was used to simulate the raw data. Noise was introduced to an equivalent SNR of 10 dB. The simulated noisy raw data was analysed using the two-step MUSIC algorithm (Sect. 3). The Input DOA was located at 0° azimuth and 75.5° elevation. At this SNR, noise-induced ambiguities are clearly visible. The probability that the output is associated with the input is 79%.

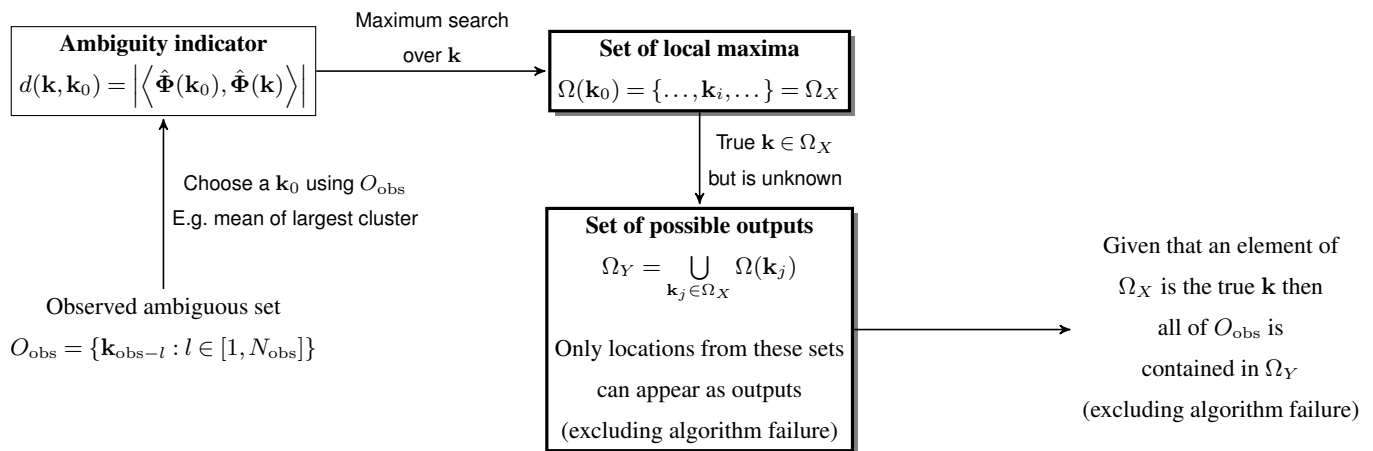


Figure 3. Overview of relation between ambiguity sets.

To account for a limited DOA determination accuracy, we choose an inclusion distance s in the wave vector ground projection plane. This distance determines the region around **all ambiguities** an ambiguity, as well as the true direction, within which we consider that particular ambiguity "chosen" by the algorithm. Thus, in the discretisation process, outputs will be considered as associated to either an ambiguity or the true DOA, otherwise they have no association.

Practically, if

$$(k_{ix} - \tilde{k}_x)^2 + (k_{iy} - \tilde{k}_y)^2 < s^2, \quad (16)$$

then the sample $\tilde{\mathbf{k}}$ is counted towards the probability P_i for output point \mathbf{k}_i assuming true input \mathbf{k}_0 . The samples which cannot
 225 be associated with any inclusion region are considered as algorithm failures, i.e. $P_f = 1 - \sum_i P_i$.

We are interested in the ~~misclassification~~ miss-classification and algorithm failure probability. We examine this by regarding
 the source as a variable j and constructing a discrete conditional probability $\mathcal{P}(\text{output } i | \text{input } j) = P_{ij}$ as a function of both
 source and output location, i.e. only the rows i sum to 1.

Even though ambiguities are not necessarily transitive relations, as mentioned in Sect. 2.1, there may still be some overlap
 230 in the inclusion regions when we define them as $\mathbf{k}_i \in \Omega(\mathbf{k}_j)$. We therefore need to spend some thought on how to practically
 discretise the problem. If we consider the usage of the simulations as a tool for evaluating a set of ambiguous observations
 $O_{\text{obs}} = \{\mathbf{k}_{\text{obs}-l} : l \in [1, N_{\text{obs}}]\}$. Then one can choose a \mathbf{k}_0 using this set of observations, by e.g. picking the mean of the largest
 cluster or picking the $\mathbf{k}_{\text{obs}-l}$ with the largest SNR.

Assuming that we have chosen an echo from the target and that our models are representative, then either \mathbf{k}_0 or one of its
 235 ambiguities $\Omega(\mathbf{k}_0)$ is the true source. Consider that an ambiguity $\mathbf{k}_i \in \Omega(\mathbf{k}_0)$ would have an ambiguity $\mathbf{k}_h \in \Omega(\mathbf{k}_i)$ which is not
 part of our original set $\mathbf{k}_h \notin \Omega(\mathbf{k}_0)$. The probability that \mathbf{k}_h is the source is zero as it could not have generated our observation
 \mathbf{k}_0 .

To provide a set of input and output wave vectors that accounts for all possible true \mathbf{k} , two separate sets of points Ω_X and Ω_Y
 should be formed. The process of constructing these sets is illustrated in Fig. 3. This is useful when quantitatively evaluating
 240 measurements as the same set Ω_Y of output regions i can be used for all simulation inputs j from the set Ω_X . The set Ω_Y is
 chosen as the collected set of all ambiguities to the simulated sources, i.e. $\Omega_Y = \bigcup_j \Omega(\mathbf{k}_j) : \mathbf{k}_j \in \Omega_X$.

Practically, consider several sets of ambiguous measurements from independent events, $O_{\text{obs}-i}, O_{\text{obs}-i+1}, \dots$ analysed using
 the methods proposed here. If the individual ambiguity sets $\Omega(\mathbf{k}_j)$ consistently do not explain the clusters of measured output
 wave vectors, there is a high probability that either the applied models are wrong or other effects are influencing the DOA
 245 determination. These effects could be radar phase calibration issues (e.g. Chau et al., 2014), antenna malfunctions or erroneous
 phenomena models (e.g. multiple simultaneous signals, signal interference, wave diffraction).

There are some practical consideration when implementing the construction of Ω_X and Ω_Y : duplicate locations should not
 be included in Ω_Y . These are handled by removal based on closeness in relation to the inclusion radius. The ordering of the
 sets Ω_X and Ω_Y are so that the first elements of Ω_Y correspond to the elements of Ω_X for clarity when examining simulation
 250 results.

Using the definitions for Ω_X and Ω_Y we ~~can~~ represent the probability P_{ij} as a matrix, excluding all non-relevant association
 probabilities. Taking a second look at Fig. 2, we one can imagine how a column of this matrix would be constructed. For each
 DOA in Ω_Y we count the ~~outputs that are output~~ inside its inclusion radius. This ~~The probability P_{ij} is this~~ number divided
 by the total number of samples ~~is the probability P_{ij}~~ . For the particular example in Fig. 2, the probability that the output is
 255 associated with the true input is 79%.

The columns of the matrix P_{ij} describe different DOA inputs for the simulation and its rows describe the probability that the
 DOA determination algorithm outputs a location as the result. The most desirable form of this matrix would be a diagonal unit

matrix, i.e., given true input j the DOA algorithm always finds the corresponding location as the output. Unfortunately, this is not always the case as this probability matrix is a function of the SNR, $P_{ij}(\text{SNR})$.

260 The error of the probability matrix P_{ij} estimations can be determined using Bernoulli distributions. The discretization can be viewed as a set of Bernoulli distributions that defines a success as: "the output DOA fall into the inclusion region" and a failure as "it did not". Then, we can measure the probability parameter P_{ij} for region and Bernoulli distribution i given input j through the fraction of samples inside that region out of all samples, i.e. \tilde{P}_{ij} . This estimator's variance $\text{var}(\tilde{P}_i)$, i.e. the accuracy of estimation, can be approximated by substituting the distribution variance with the measured Bernoulli variance and applying
 265 the central limit theorem

$$\text{var}(\tilde{P}_{ij}) \approx \frac{\tilde{P}_{ij}(1 - \tilde{P}_{ij})}{N_s}, \quad (17)$$

where N_s is the number of samples. This estimator variance has an upper limit where the parabola is maximum at $\tilde{P}_i = 0.5$. As such, the largest estimator standard error is $\sqrt{(\frac{0.25}{N_s})}$. Using 1000 samples, the largest error in probability is $\sqrt{(\frac{0.25}{1000})} \approx 1.6\%$.

2.6 Bayesian inference

270 It is generally not advisable to use data that is ambiguous. Quantitatively describing when data is "too ambiguous" for further usage is one of the goals of this study. For example, as illustrated in Fig. 2, which represents a simulation of a measured event, the event could be analysed given that enough independent echoes were measured. The reason why the event is usable is that the simulation shows that the true direction has by far the highest output probability. This means that one can pick the largest "cluster" of output DOAs and conclude that this probably represents the true DOA. However, for more complex radar systems
 275 and other input DOAs, the situation would look different. This line of reasoning also does not give us a quantitative confidence in our choice of true DOA.

If there is a need to analyse ambiguous data we suggest a Bayesian approach. As an example, let us return again to the simulation presented in Fig. 2. We argued using the simulation results that given enough independent measurements of such an event, the measurements could be used to infer the true DOA of the target. Bayesian inference generalizes this type of
 280 argumentation by optimally using all available information to assign probabilities to all possible true input DOAs.

Given a model with parameters \mathbf{x} that represents an event which has generated some observations D , Bayesian inference can be used to find the probability distribution of possible model parameters given the observed data, i.e. $\mathcal{P}(\mathbf{x}|D)$. This distribution is called the posterior. Here $|$ indicates conditional probability, i.e. $\mathcal{P}(A|B)$ is read as "the probability of A given B ". The posterior is calculated through the use of Bayes' theorem,

$$285 \quad \mathcal{P}(\mathbf{x}|D) = \frac{\mathcal{P}(D|\mathbf{x})\mathcal{P}(\mathbf{x})}{\mathcal{P}(D)}. \quad (18)$$

The $\mathcal{P}(\mathbf{x})$ term is called a prior probability, i.e. it describes what we think the probability distribution of possible model parameters is before any observations. One can view Eq. 18 as updating the prior distribution by including the knowledge gained from the new observations D . The $\mathcal{P}(D|\mathbf{x})$ term describes how probable the observed $(D|\mathbf{x})$ is given the model parameters

\mathbf{x} , commonly called the likelihood function in the Bayesian inference community. Finally, the term $\mathcal{P}(D)$ can be viewed as a
 290 normalization constant. It is commonly referred to as the prior predictive distribution, as it describes the probability of the data
 prior to updating our belief.

This approach is compatible with the problem at hand. Assuming the matrix of probabilities P_{ij} is calculated and known,
 the probability of observing \mathbf{k}_i given the input \mathbf{k}_j is exactly given by P_{ij} . Therefore,

$$\mathcal{P}(D|\mathbf{x}) = \mathcal{P}(\mathbf{k}_i|\mathbf{k}_j) = P_{ij}. \quad (19)$$

295 For the first observed DOA, the prior is uniform over all \mathbf{k}_j , i.e.

$$\mathcal{P}(\mathbf{k}_j) = \frac{1}{N_I}, \quad (20)$$

where N_I is the number of columns in P_{ij} , i.e. the size of Ω_X . If we observe $i = a_1$ as the first calculated DOA we can find
 the posterior as

$$\mathcal{P}_1(\mathbf{k}_j) = \frac{P_{a_1 j}}{\sum_{j=1}^{N_I} P_{a_1 j}}. \quad (21)$$

300 If subsequent DOA's are observed, we update the probability distribution over the model parameters by setting the last posterior
 as our prior and applying the same formula,

$$\mathcal{P}_x(\mathbf{k}_j) = \frac{P_{a_x j} \mathcal{P}_{x-1}(\mathbf{k}_j)}{\sum_{j=1}^{N_I} P_{a_x j} \mathcal{P}_{x-1}(\mathbf{k}_j)}. \quad (22)$$

If the observations a_x are done at different SNRs, the P_{ij} matrix should be allowed to change for every update x as $P_{ij}(\text{SNR}_x)$.

This method may be able to infer the true direction even in very ambiguous data. At the very least, this method provides a
 305 probability distribution over the possible directions, as exemplified in Sect 5.

2.7 Ambiguous measurement simulation

A method to investigate whether the Bayesian approach makes a significant improvement on analysis is measurement sim-
 ulation. The matrix P_{ij} describes the probability of the DOA determination generating the output indexed i given a noisy
 measurement of the true input DOA indexed j . We can thus simulate measurements as a multinomial distribution where the
 310 distribution probabilities are given by a column j of the P_{ij} matrix. Sampling this multinomial distribution will give a set of n
 simulated measurements as a list of location indices (i.e. output DOAs). Given this list of indices, Eq. 22 can be applied to cal-
 culate the most probable input given the simulated data without running the DOA determination algorithm. We can repeat this
 process to get a simulated distribution for the posterior $\mathcal{P}_x(\mathbf{k}_j)$. This distribution is what we would expect to see as inference
 results from a measurement series of n points given some true input. This distribution is useful for evaluating both the method
 315 itself and the radar system as it contains the probability of Bayesian inference finding the true input. This information can thus
 also provide the minimum SNR and measurement number needed to achieve a desired success rate in DOA determination,
 assuming the P_{ij} matrices accurately model reality.

2.8 Impact of phase offsets

Effects like mutual coupling, errors in cable lengths, and other hardware related issues can introduce phase errors in radars
320 (Chau and Clahsen, 2019). In Appendix A we show that phase offsets on the radar channel level do not affect ambiguity
dynamics if taken into account in the DOA analysis. If phase offsets are unknown they affect the accuracy of the DOA deter-
mination and the ambiguity dynamics.

There has been extensive work done to determine phase offsets as a whole on radar channels (e.g. Chau et al., 2014; Chau
and Clahsen, 2019) but we have found no work that has empirically measured or modeled the phase offsets of individual
325 antennas within a subgroup for the radars examined here. Therefore we cannot simulate a realistic distribution of phase errors
within subgroups.

To examine the impact of phase errors on the antenna level within subgroups, we performed a pair of MC simulations for
the MU radar subgroup model. As inputs the Ω_X set for \mathbf{k}_I , as given in Sec. 5, was used. For each antenna a random phase
error between -45° and 45° was introduced. Then, a MC simulation at an SNR of 3 dB was performed for both the phase error
330 model and the standard model. The probability matrix for each of these simulations were calculated and the difference between
them examined. There was practically no difference in the probability matrices.

It should be noted that in this test the phase offsets that generated the simulated noisy signal were also included in the
MUSIC analysis model. Finally, we ran two MC simulations at 5 dB SNR for the MU subgroup model, using \mathbf{k}_I and \mathbf{k}_{II} as
input DOAs. In these simulations the noisy signal was generated with channel phase offsets measured using a technique similar
335 to the one presented in Chau and Clahsen (2019) but analysed using no phase offsets. For these two cases, the uncorrected phase
offsets did not impact the ambiguity dynamics, but it did introduce a small error in the DOA determination accuracy. As such,
the results presented here are applicable in general when phase errors are measured or modeled and possibly even when not
measured or modeled. Further examination of the impact on ambiguities of unknown phase errors is desirable but outside the
scope of the current study.

340 3 DOA determination

For the purpose of consistency and simplicity we have used the same DOA determination method for all radar systems exam-
ined: the MUSIC algorithm (Schmidt, 1986). This method allows for an arbitrary sensor response model Φ and can thus be
applied on all systems. MUSIC is practically equivalent to beam forming DOA methods but with reduced variance due to the
subspace approach. We here give a short overview of how we have applied the MUSIC method.

345 We define a measured sensor response as the complex vector $\mathbf{x} \in \mathbb{C}^N$. The sensor response model in Eq. 1 refers to a so called
decoded signal. The decoded signal is the signal coherently integrated over all temporal samples of a radar pulse. However,
the lowest level of raw data also contains these temporal samples of the radar pulse. Given M temporal samples of the coded

pulse, the measurement matrix then consists of N rows and M columns as

$$X = \begin{pmatrix} \mathbf{x}_1 & \mathbf{x}_2 & \dots & \mathbf{x}_M \end{pmatrix}. \quad (23)$$

350 The correlation matrix R of our measurements is calculated using matrix algebra as

$$R = \frac{1}{M} X X^\dagger. \quad (24)$$

The correlation matrix consists of coherently integrated channel-to-channel phase differences over the temporal samples. The eigenvalues of the correlation matrix correspond to signal powers and the eigenvectors corresponding to the largest eigenvalues span the signal subspace (Schmidt, 1986). If there is noise, the eigenspace spans the entire sensor configuration space, otherwise
 355 it only spans the signal subspace. First, we extract the eigenvectors \mathbf{P}_i and eigenvalues λ_i of the correlation matrix using standard linear algebra methods. Then, assuming one signal subspace dimension, i.e. one signal from one direction, we define the noise subspace as the column space of

$$Q = \begin{pmatrix} \dots & \mathbf{P}_{j-1} & \mathbf{P}_{j+1} & \dots \end{pmatrix}, \quad (25)$$

where \mathbf{P}_j corresponds to the largest eigenvalue $\lambda_j = \max(\{\lambda_i : i \in [1, M]\})$. This eigenvector represents the signal subspace.
 360 MUSIC is a multiple signal classification method. If there are multiple signals present in the data, the second eigenvector and eigenvalue is associated with the second strongest signal, etc. As the column vectors of Q form an orthonormal basis, consider the space

$$\mathbb{Q} = \text{span}\{\mathbf{P}_1, \dots, \mathbf{P}_{j-1}, \mathbf{P}_{j+1}, \dots, \mathbf{P}_M\}. \quad (26)$$

The scalar projection function P into this linear subspace \mathbb{Q} is

$$365 P_{\mathbb{Q}}(\mathbf{x})^2 = \sum_{i=1, i \neq j}^M \langle \mathbf{P}_i, \mathbf{x} \rangle_{\mathbb{C}^M}^2 = |Q^\dagger \mathbf{x}|^2. \quad (27)$$

The space \mathbb{Q} represents the noise, thus any space orthogonal to \mathbb{Q} is a signal. The projection of a vector onto an orthogonal space is zero, thus we are searching for vectors \mathbf{x} that minimises $P_{\mathbb{Q}}(\mathbf{x})$.

We write the projection function in terms of matrix operations as

$$P_{\mathbb{Q}}(\mathbf{x})^2 = |Q^\dagger \mathbf{x}|^2 = (Q^\dagger \mathbf{x})^\dagger (Q^\dagger \mathbf{x}) = \mathbf{x}^\dagger Q Q^\dagger \mathbf{x}. \quad (28)$$

370 Normalizing the projection with respect to the input vector norm and inverting, we maximise instead of minimise, and find the familiar MUSIC function. As we have a model for \mathbf{x} as a function of DOA, we set $\mathbf{x} = \Phi(\mathbf{k})$ and find

$$f(\mathbf{k}) = \left(\frac{P_{\mathbb{Q}}(\Phi(\mathbf{k}))^2}{|\Phi(\mathbf{k})|^2} \right)^{-1} = \frac{\Phi(\mathbf{k})^\dagger \Phi(\mathbf{k})}{\Phi(\mathbf{k})^\dagger Q Q^\dagger \Phi(\mathbf{k})}, \quad (29)$$

which is the form usually recited in literature. This function needs to be maximized by an appropriate method to find the sensor response $\Phi(\mathbf{k})$ that best matches the detected signal, thereby also determining the DOA, \mathbf{k} , of the signal.

375 As Eq. 29 takes the the scalar projection onto the signal complement space, the function is invariant to the orientation of the vector with respect to the signal subspace basis. Thus, the definition in Eq. 6 is appropriate to describe the ambiguities of MUSIC.

We have chosen to apply a two-step maximization method. First, a finite grid search over all possible \mathbf{k} was applied. Then, the maximum found during this grid search was used as an initial condition for a gradient ascent applied on $\nabla f(\mathbf{k})$ to find the
380 peak point. Finally, the peak value is used as output, i.e. as the determined DOA of the signal.

However, there is no guarantee that the initial grid search will always be able to identify the correct slope as an initial condition for the gradient ascent. If the peak width is smaller than the grid size any slope may be found instead. To solve this problem we also implemented an option of running multiple gradient ascents in parallel. When this option is enabled, instead of using only the maximum point from the grid search as a start value, the N largest values that are separated from each other
385 by at least δX in k_x, k_y space are used. The separation condition ensures that no two start points are located on the same slope. These N start points are explored by a gradient ascent and the largest peak among them is chosen as the algorithm output.

4 Radar systems

The sensor response for all radars covered in this study were modeled using two different models, a simplified model

$$\Phi(\mathbf{k}) = \begin{pmatrix} An_1 e^{-i\langle \mathbf{k}, \mathbf{r}_1 \rangle_{\mathbb{R}^3}} \\ \vdots \\ An_N e^{-i\langle \mathbf{k}, \mathbf{r}_N \rangle_{\mathbb{R}^3}} \end{pmatrix}, \quad (30)$$

390 where n_i is the number of antennas summed to that radar channel. And a model using the subgroup gain patterns

$$\Phi(\mathbf{k}) = \begin{pmatrix} Ag_1(\mathbf{k}) e^{-i\langle \mathbf{k}, \mathbf{r}_1 \rangle_{\mathbb{R}^3}} \\ \vdots \\ Ag_N(\mathbf{k}) e^{-i\langle \mathbf{k}, \mathbf{r}_N \rangle_{\mathbb{R}^3}} \end{pmatrix}, \quad (31)$$

$$g_j(\mathbf{k}) = \sum_{l=1}^{N_j} e^{i\langle \mathbf{k}, \mathbf{r}_j - \rho_{jl} \rangle_{\mathbb{R}^3}}. \quad (32)$$

The exceptions are the Jones type radar systems where there are no subgroups but only single antennas. As previously mentioned, in these models \mathbf{r}_i indicate the locations of individual antennas or the geometric centers of the sub-arrays, i.e. the phase
395 centers.

In this study we have assumed that the antennas have omnidirectional gain. This is of course not the case, as mentioned in Sect. 2, but this assumption has no impact on the current study. As all radar systems examined have the same antennas

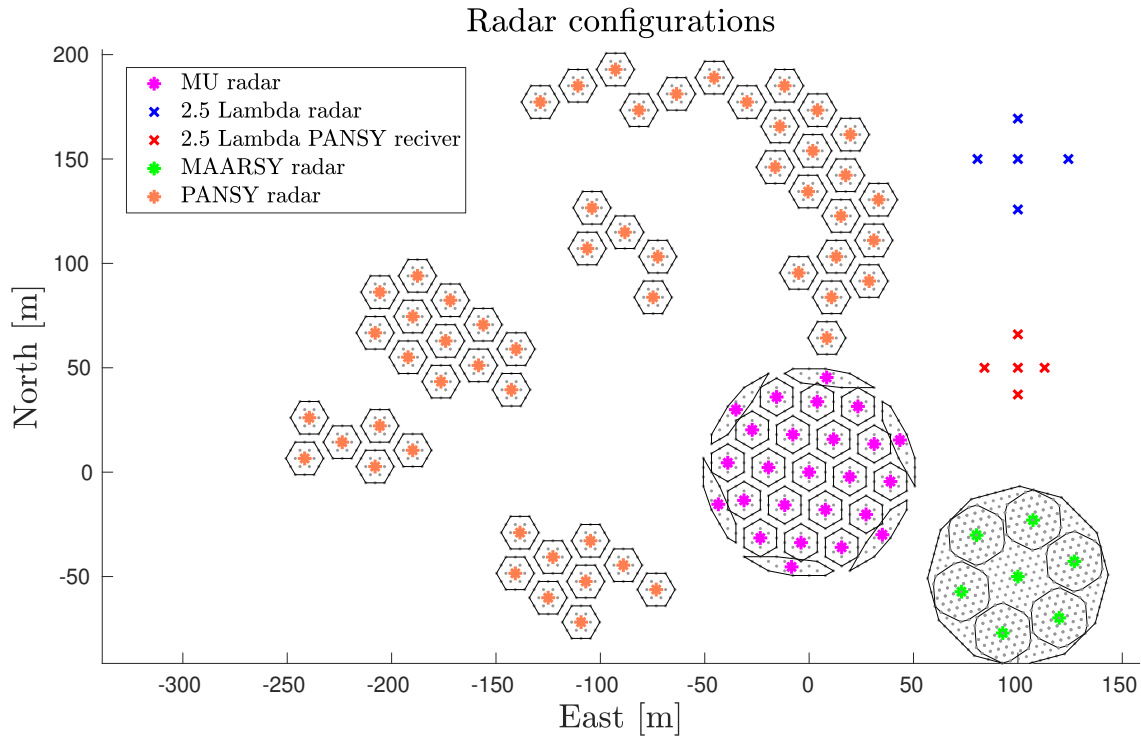


Figure 4. The different radars considered in the DOA determination study. For the radars which consists of subgroups of antennas the subgroup centers are colored radar-specific while antennas and subgroup borders are always grey and black. The Jones 2.5λ radars are single antenna channel radars so here colored markers indicate antennas.

throughout the system, the individual gain function for an antenna cancels in any algorithm that is invariant to signal amplitude. However, in the implementation of a data analysis pipeline it is important to implement the individual antenna gain pattern γ and the subgroup generated gain patterns in the sensor response model to be able to determine the radar cross section correctly.

We hereafter refer to the model in Eq. 30 as the **phase center model** and the model in Eq. 31 as the **subgroup model**.

In Fig. 4 the antenna positions of all examined radars are illustrated so that their individual configurations and sizes can be compared.

4.1 Jones 2.5λ radar

Radar systems designed for studying meteor trail echoes commonly consist of a wide angle (all-sky) transmitter system and an interferometric receiver system (e.g. Jones et al., 1998; Hocking et al., 2001).

The receiver system design is beset by two problems (Jones et al., 1998): that antenna spaced more than $\lambda/2$ apart give rise to ambiguities in the DOA, and that antennas spaced less than $\lambda/2$ apart give rise to strong mutual impedance. The so-called Jones 2.5λ radar configuration is an elegant solution suggested by Jones et al. (1998) as a remedy to the situation. The solution

410 consists of using five antennas, one central antenna and two spaced by 2.5λ and 2.0λ in each of the two perpendicular cardinal directions (cf. Fig. 4).

As described by Jones et al. (1998), the phase measurements at the outer antennas relative to the central antenna can ideally be used to calculate an unambiguous determination of the echo DOA, taking advantage of the fact that the internal antenna distances to the central antenna differs by $\lambda/2$. Furthermore, the phase difference of antennas with 4.5λ spacing is used to give
415 better angular precision at the cost of ambiguous DOA, the most probable solution of which is then selected using the $\lambda/2$ phase difference.

Holdsworth (2005) investigated the Jones antenna configuration and found that the usage of 2.5 , 3 and 5.5λ spacings could produce more accurate echo DOA. Younger and Reid (2017) developed the concept further and presented a solution which utilise all possible antenna pairs of a meteor radar antenna configuration, similarly to the DOA calculations using MUSIC in
420 this paper. In addition to providing results in excellent agreement with the original interferometric algorithm by Jones et al. (1998), the method presented by Younger and Reid (2017) as well as the MUSIC algorithm allows for different layouts.

The Jones antenna configuration has remained predominant in meteor radar installations and is often referred to as removing (in principle) any angular ambiguities (Hocking et al., 2001). However, as was pointed out already by Jones et al. (1998), the determination is sensitive to noise and only unambiguous if the SNR is large enough. The original simulations by Jones
425 et al. (1998) showed that the method started to produce incorrect apparent echo directions for elevations greater than 30° when the SNR was below 17 dB, but that at the same time the fraction of these was small down to about 10 dB. The standardized SKiYMET software meteor detection data contains an ambiguity level classification. If the ambiguity parameter is equal to 1, the data was determined to be unambiguous, and if it is greater than 1 there is a possibility that the meteor was erroneously located (Hocking et al., 2001).

430 To our knowledge, there are no further quantitative investigations of the Jones 2.5λ radar configuration performance except for the studies mentioned above and references therein. The results of applying the method presented in this paper on the Jones 2.5λ radar to quantify noise-induced ambiguities are given in section 5.1. As the mentioned studies on ambiguities already exists, simulating a Jones 2.5λ radar also provides a good reference simulation for validation of the methods presented in Sect. 2.

435 4.2 MU radar

The 46.5 MHz Middle and Upper atmosphere (MU) radar near Shigaraki, Japan (34.85°N , 136.10°E) has a nominal peak transmitter power of 1 MW and a maximum beam duty cycle of 5%. The present setup of the MU radar hardware comprises a 25 channel digital receiver system. It was upgraded from the original setup (Fukao et al., 1985) in 2004 and is described by Hassenpflug et al. (2008). After the upgrade, the MU radar always transmit right-handed circular polarization and receive
440 left-handed circular polarization, with a phase accuracy of 2° . The output of each digital channel is the sum of the received radio signal from a subgroup of 19 Yagi antennas. The whole array consists of 475 antennas, evenly distributed in a 103 m circular aperture, with a main lobe maximum gain of 34 dB and a minimum half power beam width of 3.6° . A schematic view of the array and the subgroups is given in Fig. 4.

Early meteor head echo measurements using the original setup with four receiver channels (Nishimura et al., 2001) are not
445 investigated further in this study. The focus is instead on the current 25-channel setup, which has been used more extensively
for hard targets such as meteors (e.g. Kero et al., 2011, 2012a, b, 2013; Fujiwara et al., 2016; Kastinen and Kero, 2017).

4.3 MAARSY radar

The new Middle Atmosphere Alomar Radar System (MAARSY) was constructed in 2009/2010 on the Norwegian island
Andøya (69.30°N, 16.04°E) following similar design principles as the MU radar. It is a monostatic radar operated at 53.5 MHz
450 with an active phased array antenna consisting of 433 Yagi antennas (Latteck et al., 2010). The antennas are, similarly to the
MU radar, arranged in an equilateral triangle grid with 0.7λ (4 m) spacing, forming a 90 m circular aperture. This results in a
rather symmetric radar beam with a maximum directive gain of 33.5 dB and a minimum half power beam width of 3.6° . Each
individual antenna is connected to a transceiver with independent phase control and output power up to 2 kW, enabling flexible
beam forming, beam steering and approximately 800 kW peak transmitter power with 5% duty cycle.

455 The smallest MAARSY subarray unit consists of seven antennas distributed in a hexagonal pattern as illustrated in Fig. 5.
The receiver system currently allows for 16 separate channels. Early meteor head echo observations with MAARSY used eight
channels which were defined according to Fig. 4, where seven of the channels consisted of the combined input from seven
subarrays (i.e. 49 antennas) and the eighth channel contained the combined input from all antennas (Schult et al., 2013). Later
meteor head echo observations have made use of the alternative MAARSY configuration visualised in Fig. 5 (Schult et al.,
460 2017).

The radiation pattern of MAARSY have been studied and validated through observations of cosmic radio sources (Renkwitz
et al., 2012, 2013), scattering of a sounding rocket's payload (Renkwitz et al., 2015) and meteor head echoes (Renkwitz et al.,
2017). Methods have also been developed to calibrate and validate the measured phases of the individual channels using cosmic
radio noise and meteor head echoes (Chau et al., 2014).

465 4.4 PANSY radar

The Program of the Antarctic Syowa MST/IS radar (PANSY) is a Mesosphere–Stratosphere–Troposphere/Incoherent Scatter
(MST/IS) radar located at the Japanese Syowa Station (69.01°S, 39.59°E) in the Antarctic (Sato et al., 2014). The first subarrays
of the PANSY radar were installed in 2011. The first continuous observations of Polar mesospheric summer echoes were made
with a single subarray in January-February 2012. Due to snow accumulation in the originally symmetric antenna field consisting
470 of 1045 crossed Yagi antennas summed into 55 channels, several of the subarrays were moved to higher ground as illustrated
in Fig. 4. This is the antenna configuration we have used in the simulations.

PANSY operates on a center frequency of 47 MHz and with a peak power of 500kW and 5% duty cycle. The radar is a
challenge for DOA determinations as the subgroups are located at different altitudes and partially disjoint, and have to be
moved or intermittently be disconnected from the system depending on snow accumulation conditions. Even the antennas
475 within subgroups are elevated non-symmetrically. Currently the antennas are distributed in altitudes ranging between -2 and
+8 meters from the reference plane.

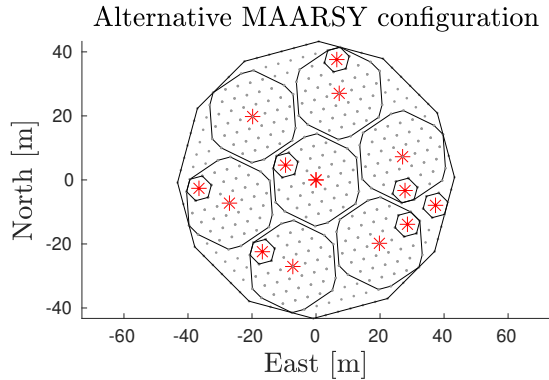


Figure 5. An alternative configuration of MAARSY subgroups used as radar channels to the one illustrated in Fig. 4. In this configuration 15 channels are used instead of 8 as to include the information from smaller but closely located hexagonal groups. Thus producing shorter baselines for less ambiguous interferometry (Schult et al., 2017).

In 2017, a peripheral antenna array for detecting field-aligned irregularities (FAI) were installed (Hashimoto et al., 2019). This has enabled suppression of FAI echoes and increased the number of power profiles usable for incoherent scatter measurements of the polar ionosphere by more than 20%. In this paper we do not investigate the peripheral FAI array.

480 4.5 PANSY meteor radar

The PANSY radar has recently been complemented by a meteor trail echo interferometric receiver system (Taishi Hashimoto, personal communications). The antenna configuration is displayed in Fig. 4. Since the operating frequency of PANSY (47 MHz) differs from meteor radar systems (typically 35 MHz), the configuration is more compact when displayed in units of metres even though the number of wavelengths are the same. The main difference between the PANSY meteor radar receiver and the
 485 Jones 2.5λ radar is that the prior is not a planar array but that the antennas are displaced in the vertical (z) direction with up to 0.8 m, corresponding to $\sim 0.12\lambda$.

5 Results

To demonstrate the above methods we present results from numerical simulations. The next step will be applying them on measurement data. We aim to implement these methods in our data analysis pipelines for meteor head echoes measured by
 490 the MU radar and the PANSY radar in the future, as well as classify the location probability of ambiguous meteor radar trail echoes using Bayesian inference. However, the current study allows us to quantitatively evaluate how DOA determination behave with respect to SNR and qualitatively evaluate if ambiguities are relevant or not. Such results are useful in configuration and construction of pipelines.

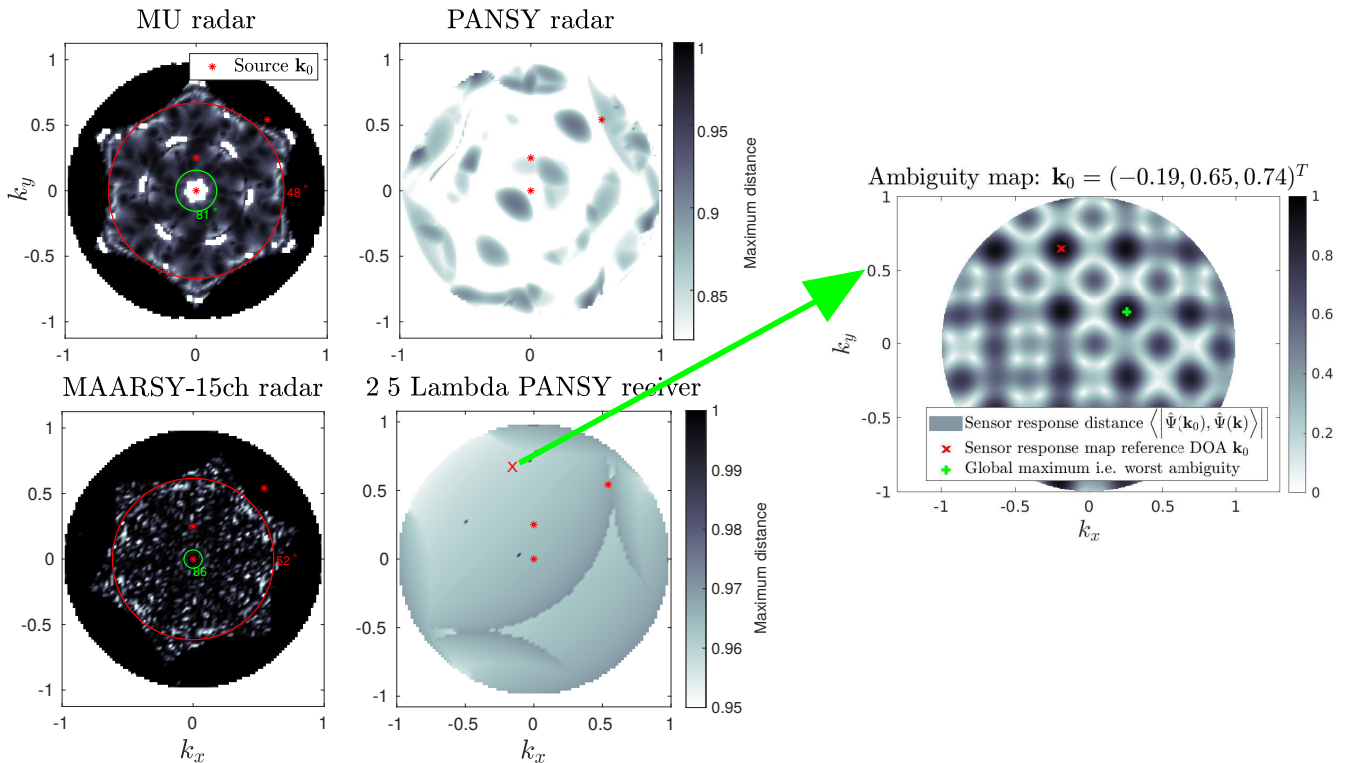


Figure 6. Map of worst ambiguity as a function of input DOA for the MU radar subgroup model, the MAARSY-15ch radar subgroup model, the PANSY subgroup model and the 2.5λ receiver model. For each \mathbf{k}_0 an ambiguity search over \mathbf{k} of $d(\mathbf{k}, \mathbf{k}_0)$, as defined in Eq. 6, was performed. The result from the ambiguity search yields $\Omega(\mathbf{k}_0)$. The ambiguity with smallest distance-largest inner product to \mathbf{k}_0 gives the distance- d value at the location \mathbf{k}_0 in the map to the left. Using the applied color scale, white indicates a better situation and black indicates a worse situation with respect to ambiguities. An example of such an ambiguity search result is shown in the rightmost panel for a particular \mathbf{k}_0 . Overlaid on these maps are red crosses illustrating the further examined source directions and concentric elevation limits described in Section 5. Note the difference in color scale between the top and bottom row.

For each of the radar systems described in Sect. 4 we have applied the methods described in Sect. 2 and 3. Three input
495 directions \mathbf{k}_0 were chosen as sources:

- I. $\mathbf{k}_I =$ Azimuth: 0° , Elevation 75.5° ,
- II. $\mathbf{k}_{II} =$ Azimuth: 0° , Elevation 90° ,
- III. $\mathbf{k}_{III} =$ Azimuth: 45° , Elevation 40° .

For each of these chosen sources the following steps were performed:

- 500 – Determine all ambiguities using 1000 starting conditions according to the method outlined in Sect. 2.1. This generates the Ω_X and Ω_Y sets.

- Run an MC simulation of 500 samples for each input direction in Ω_X at all SNR levels, according to the method outlined in Sect. 2.4. An appropriate range of linearly spaced SNRs in decibel was used to capture the transition from stable DOA determination to complete algorithm failure.
- 505 – Discretise the MC results into probability matrices P_{ij} using the sets Ω_X and Ω_Y according to Sect. 2.5, using an inclusion radius of $s = 0.07$.
- If applicable, simulate measurements according to Sect. 2.7 and calculate Bayesian inference distributions according to Sect. 2.6.

The ambiguity dynamics change as a function of input DOA for all systems but the planar Jones 2.5λ configuration. A complete overview of the ~~distance~~-indicator function $d(\mathbf{k}, \mathbf{k}_0)$ is therefore four dimensional. To visualise the ambiguity dynamics, a grid of \mathbf{k} -vectors over all possible \mathbf{k}_0 was used and only the worst ambiguity was saved for each grid point. I.e., on each grid-point \mathbf{k}_0 all ambiguities were calculated and the ~~minimum distance~~-maximum value ambiguity was saved for that direction.

This kind of map shows which source directions the radar is able to resolve well and which directions it cannot uniquely determine. While it does not illustrate the morphology of ambiguities, it does show the qualitative connection between input DOA and limiting SNR. The white areas are regions where no ambiguities were found using the selected algorithm settings.

The analysis results for each of the radar systems (except the planar Jones 2.5λ radar) are illustrated in Fig. 6. Overlaid on these maps are red crosses illustrating the chosen source directions further examined. These input DOAs \mathbf{k}_{I-III} were chosen to cover a wide range of "worst ambiguity" and elevation angle. The same three directions were selected for all systems to enable cross comparisons. We did not take population models or detection probabilities into consideration when choosing these input directions.

Additionally, on the maps for the MU radar and the MAARSY-15ch radar, two elevation limits are shown as two concentric circles. The inner circle represent the elevation above which DOA determination is practically unambiguous. The outer circle illustrates the elevation below which unambiguous DOA determination is practically impossible.

525 Before application on measurement data one should validate that the sets Ω_X and Ω_Y are predicting the behaviour of the MC simulations so that unexpected dynamics introduced by the DOA determination algorithm itself are not disregarded. If the measurement data cannot be explained by MC simulation, the sensor response model or the phenomenon model are most likely not representative.

5.1 Jones 2.5λ radar

530 First, we report results for the Jones 2.5λ radar as this is the simplest system examined in the study. Furthermore, trivial and previously published results exist for reference (e.g. Jones et al., 1998; Chau and Clahsen, 2019).

Following the steps outlined above, the resulting DOA sets Ω_X and Ω_Y for \mathbf{k}_I , \mathbf{k}_{II} and \mathbf{k}_{III} were determined. As expected, the generated ambiguity maps indicate that the Jones configurations has prominent ambiguities at ± 0.43 in the directional cosine along both of the array axes. As this is a simple radar system, these ambiguities can be found with conventional methods

2.5 Lambda radar [Ambiguity set 1]: MC MUSIC DOA determination

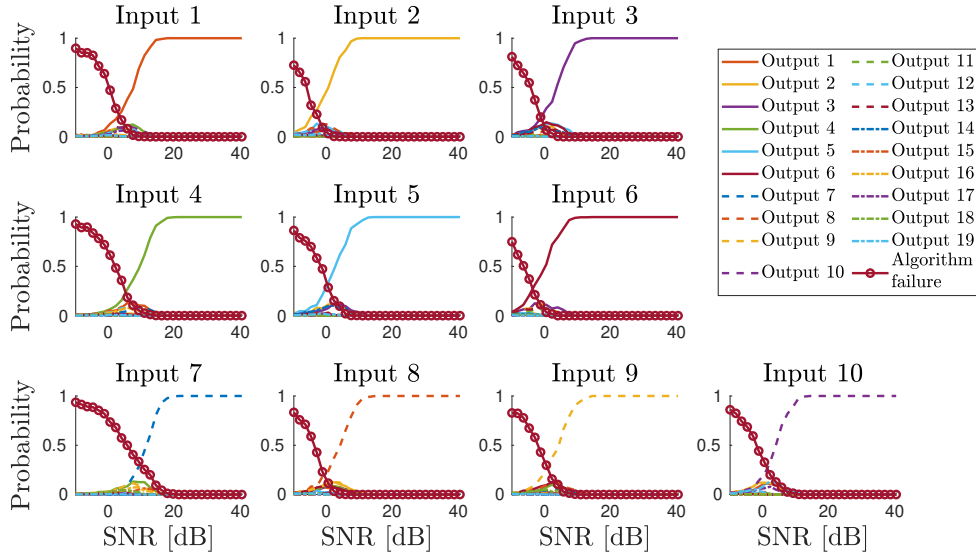


Figure 7. The discretised output DOA distribution as a function of SNR and input DOA for the Jones 2.5λ radar, when using \mathbf{k}_I to generate Ω_X and Ω_Y . Output 1-5-1-10 ($\subset \Omega_Y$) correspond to Input 1-5-1-10 (Ω_X), while Output 6-29-11-19 ($\subset \Omega_Y$) are scattered according to the second degree ambiguities. Numerical values of Input 1-5-1-10 are given in Table 1, Jones 2.5λ , I.1-5-10. The DOA outputs that do not fall into any discretisation region are classified as algorithm failure.

535 equivalent to the Nyquist-Shannon sampling theorem (Jones et al., 1998). These ambiguities can also be found by analytically solving Eq. B1 from Appendix B. Any ambiguity map for the Jones system is simply a translation in \mathbf{k} space of the map at zenith, as shown in Appendix B.

A series of MC simulations were performed using the set Ω_X as input DOAs. The probability P_{ij} was calculated for each simulated SNR using the set Ω_Y . The P_{ij} matrix elements as a function of SNR are illustrated in Fig. 7 for the source \mathbf{k}_I .
 540 One panel in Fig. 7 illustrates a column of the P_{ij} matrix and each curve represents a row of the matrix. Output 1-5-1-10 ($\subset \Omega_Y$) correspond to Input 1-5-1-10 (Ω_X), while Output 6-29-11-19 ($\subset \Omega_Y$) are scattered according to the second degree ambiguities. Numerical values of Input 1-5-1-10 are given in Table 1, Jones 2.5λ , I.1-5-10.

As expected, the results for \mathbf{k}_{II} and \mathbf{k}_{III} (not shown here) are practically identical (as the ambiguity maps are identical) to the ones illustrated in Fig. 7, but shifted in SNR space. The relative SNR shifts are due to array gain differences and are given
 545 numerically in Table 1.

Fig. 7 shows the region where noise-induced ambiguities are relevant. For example, the DOA of Input 1 is always correctly determined above 10 dB SNR. Noise-induced ambiguous solutions appear between -10 dB and 10 dB SNR. At lower SNR, the algorithm returns approximately uniformly distributed results classified as algorithm failure. Different input directions have different thresholds as shown in Table 1. For most directions 10 dB array SNR is not sufficient for 99% confidence.

Ambiguities for the MU radar

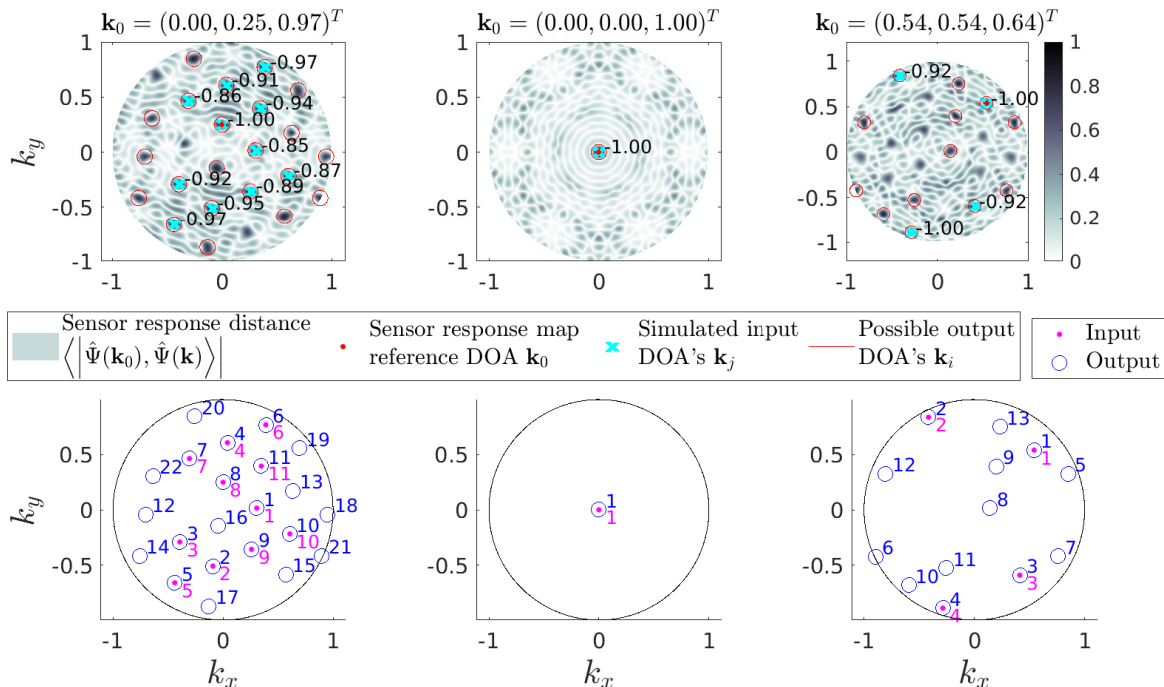


Figure 8. Ambiguity analysis summary illustration for the MU radar using the subgroup model. The three columns, from left to right, represent the source DOAs \mathbf{k}_I , \mathbf{k}_{II} and \mathbf{k}_{III} . For each column, the top row consists of sensor response distance-inner product $d(\mathbf{k})$ maps calculated using Eq. 6. The value of $d(\mathbf{k})$ ranges from 0 to 2-1 as Eq. 6 effectively describes the distance-between-two-points-norm of the projection of one point onto another, thus the maximum distance is 2-1. Overlaid on the map are the reference DOA \mathbf{k}_0 , the simulated input DOA set $\mathbf{k}_j \in \Omega_X$ and the possible output DOA set $\mathbf{k}_i \in \Omega_Y$. The bottom row shows an indexing map for Input-Output locations.

550 Following the method outlined in Sect. 2.6, we have generated a simulated series of observations for the Jones 2.5λ radar and analysed that series with Bayesian inference to find $\mathcal{P}_x(\mathbf{k}_j)$. We have examined how often the Bayesian inference $\mathcal{P}_x(\mathbf{k}_j)$ was able to correctly identify the true input by assigning it the largest probability. This gives an estimation for the ideal expected success of applying Bayesian inference on ambiguous echoes for that SNR. Repeating the process for every SNR level that was simulated, we found the probability of correct classification as a function of SNR and number of observed outputs. Generally,

555 the simulations showed that the ideal relation between needed SNR and needed observations followed an inverse relation with the number of observations.

MU radar: Sensor response model channel phase

Including subgroup gain Phase centre approximation

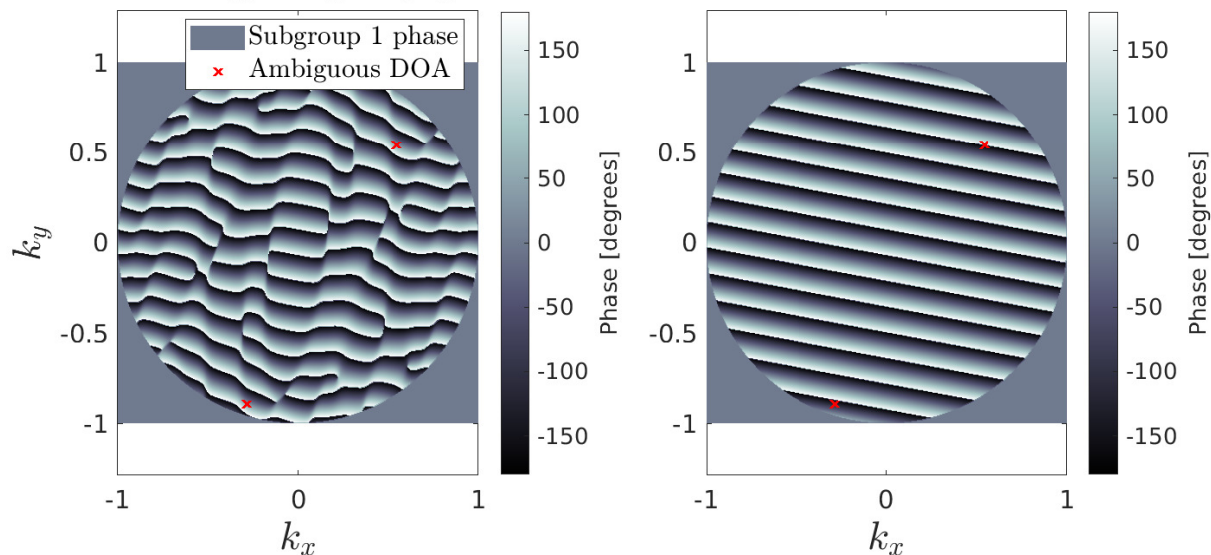


Figure 9. Comparison of the signal phase measured using the subgroup model and the phase center model of MU radar channel 1 (the outer asymmetric subgroup to the west illustrated in Fig. 4). The inclusion of the asymmetric antenna positions in the subgroup model affects the expected phase measurements of the signal as a function of wave DOA. The two red crosses mark two direction that are ambiguous in the subgroup model but not in the phase center model.

5.2 MU radar

In contrast to the Jones 2.5λ radar, the MU radar channels consists of subgroups of antennas. If all subgroups were identical and had a reflection symmetry-line, this would mathematically assure that the subarray gains do not have imaginary components and have the same dependence on input DOA. Practically, it would mean that the subarray gain patterns g_j could be omitted. However, as is illustrated in Fig. 4, the MU radar has six outer subgroups that are not symmetric nor equal. Thus, the subgroup gain will affect the normalized sensor response model and the DOA determination capabilities. Therefore we consider both of the models described in Eqs. 30 and 31.

Given the MU asymmetric subgroups, one could consider the model in Eq. 30 unphysical. Nevertheless, the phase center model has been successfully used to analyse meteor head echoes from the MU radar (Kero et al., 2012b). The reason is that the two models obviously converge towards the zenith and are very similar in the main lobe and first side-lobes as they are both models of planar arrays. Since most meteor head echo detections occur in the main lobe of the radar, only a small portion of the events are affected by the difference between the two models.

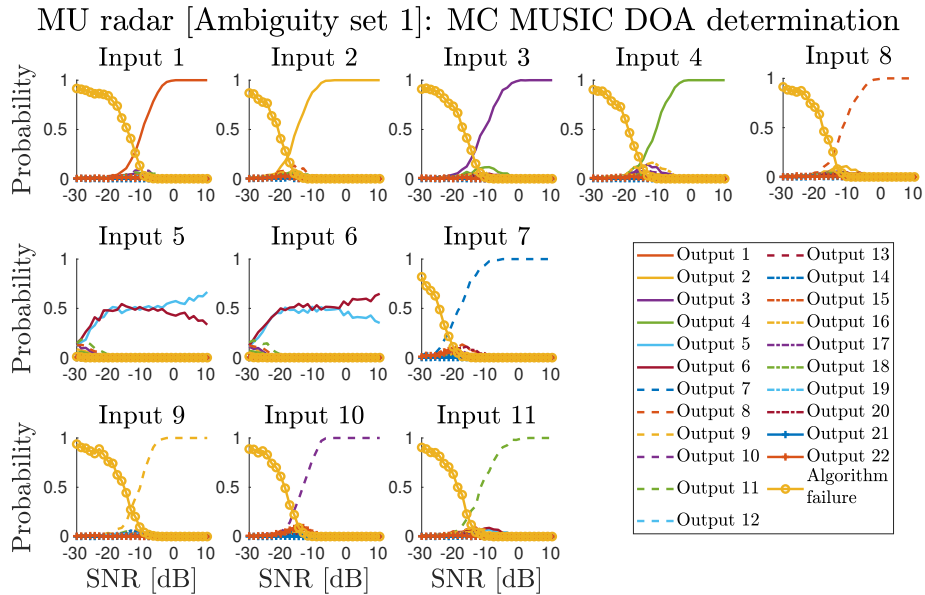


Figure 10. The discretised output DOA distribution as a function of SNR and input DOA for the MU radar, using the subgroup model and \mathbf{k}_I to generate Ω_X and Ω_Y . The numerical values of Input ~~1-7~~ 1-11 (Ω_X and corresponding to Output ~~1-7~~ 1-11) are given in Table 1, MU, I.1-~~7~~ 11.

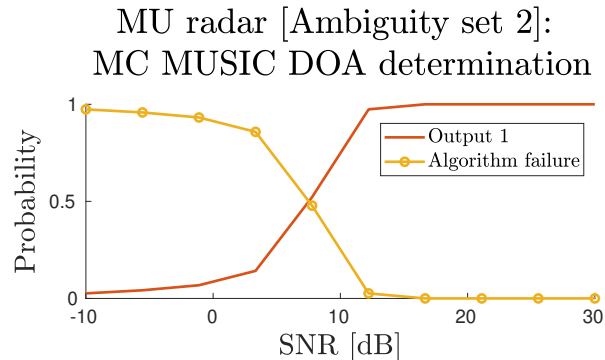


Figure 11. The discretised output DOA distribution as a function of SNR and input DOA for the MU radar, using the subgroup model where Input 1 is \mathbf{k}_{II} (Ω_X) and Output 1 is also \mathbf{k}_{II} (Ω_Y).

As the ambiguity results for the Phase centre model are close to trivial (cf. Appendix B), we do not present any ambiguity maps for that model. It is sufficient to note that there are no ambiguities with $d=0$ $d=1$ due to the geometric centers of the six outer groups breaking the symmetry of the 19 hexagonally symmetric inner groups.

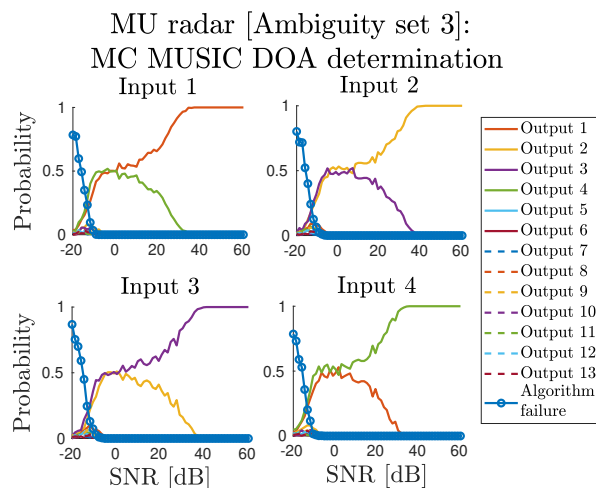


Figure 12. The discretised output DOA distribution as a function of SNR and input DOA for the MU radar, using the subgroup model and \mathbf{k}_{III} to generate Ω_X and Ω_Y . The numerical values of Input ~~1-6~~ 1-4 (Ω_X and corresponding to Output ~~1-6~~ 1-4) are given in Table 1, MU, III.1-~~6~~ 4.

The MU radar subgroup model is expected to have an ambiguity map that varies as a function of input DOA. We present maps for \mathbf{k}_I , \mathbf{k}_{II} and \mathbf{k}_{III} and the resulting DOA sets Ω_X and Ω_Y in Fig. 8 to exemplify the variability of the ambiguity map morphology in addition to the variability of the worst ambiguity (cf. Fig. 6).

575 Comparing the phase center model with the subgroup model, the DOA determination situation improves slightly for \mathbf{k}_I and \mathbf{k}_{II} as many ambiguities become less prevalent. This can be attributed to the fact that the two models diverge at lower elevations, thereby making it easier to distinguish a low-elevation DOA from a DOA near the zenith. However, For \mathbf{k}_I , the closest ambiguities basically remain at the same distance ~~$d=0.26$~~ $d=0.97$. Furthermore, for \mathbf{k}_{III} , there is even a close to perfect ambiguity (~~$d=0.00474$~~ $d=0.999988$) as illustrated by the top right panel in Fig. 8. This may appear surprising as
580 previously there were no perfect ambiguities. However, the change makes sense given the internal antenna configuration of the outer subgroups that differentiate between the ambiguities formed by the 19 inner subgroups.

The phase output of subgroup 1, the outer subgroup to the west in Fig. 4, using the subgroup model versus the phase center model is illustrated in Fig. 9. The two red crosses correspond to the two directions labeled ~~$d=0$~~ $d=1.00$ in the top right panel in Fig. 8. Here it is clearly seen that the phase have equal values for these two directions when including subgroup gain in
585 the left panel, while the phase values were very different when using the phase center approximation shown to the right. This channel is the main contributor to differentiating between these two ambiguities that appear due to the 19 inner subgroups. This highlights the advantage of numerically investigating ambiguities, either by sensor response model ~~distance-ambiguity~~ indicator maps or by MC simulation as this ambiguous DOA would probably have gone unnoticed otherwise.

As the phase centre model and subgroup model converges towards the zenith we only present MC results from the subgroup model. The summary of the MC MUSIC DOA determinations for that model is illustrated for \mathbf{k}_I , \mathbf{k}_{II} and \mathbf{k}_{III} in Figs. 10, 11 and 12, respectively.

From Fig. 10 we see trouble determining directions uniquely if they are in the "dark-zone" indicated by the MU panel in Fig. 6. The Input and Output locations are given by Fig. 8. Here, the MUSIC DOA determination is unable to select the correct output for Input ~~3 and 4~~ 5 and 6 even though there is a small difference between the signals (~~$d = 0.00474$~~ $d = 0.999988$ as mentioned previously). As these simulations were using a single starting point for the MUSIC gradient ascent, the behaviour could be caused by a narrow-peak problem. When using a fixed grid to select the starting point for the MUSIC gradient ascent, it may miss a narrow peak.

To test if a narrow peak was causing problems, we applied the parallel gradient ascent technique described in Sect. 3 when performing MC simulations for \mathbf{k}_{III} . We chose the $N = 20$ largest grid points with a minimum separation of $\delta X = 0.1$ as initial conditions for the gradient ascents. We also increased the examined SNR range to find the region in which a ~~$d = 0.00474$~~ $d = 0.999988$ ambiguity could be correctly determined. The resulting MC statistics are illustrated in Fig. 12. For targets with SNR higher than 40 dB, an unambiguous DOA determination in this region is possible. Candidates for producing such strong echoes include bolides with large radar cross section and active satellite.

As indicated by the MU panel in Fig. 6, all directions located close to the zenith are very robustly determinable. Therefore, no extensive MC simulations are needed for \mathbf{k}_{II} . Instead, we ran a set of sparse simulations in the SNR space to examine the onset of algorithm failure, illustrated in Fig. 11. In this case the onset occurs below around 12 dB SNR.

The different input locations differ significantly in the SNR needed for stable DOA determination. This SNR limit also differs with respect to the used sensor response model. As such, the MUSIC peak value is a more stable quality indicator than SNR for DOA determination. The MUSIC peak value directly describes how well the used sensor response model matches the measured signal. The MUSIC peak distribution for the MU subarray model simulations is given in Fig. 13. The simulations are the same as those illustrated in Fig. 11. In the SNR range ($\text{SNR} \lesssim 10$ dB) where the MUSIC peak value appears to be independent of SNR, the algorithm can not find any significant matches. The SNR region just above the flat section of the distribution is where ambiguities can occur. Measured echoes deviating from this relation between SNR and MUSIC peak value indicate an erroneous sensor response model.

As the MU radar is a more complex system than the Jones 2.5λ radar it might be misleading to simulate Bayesian inference and we have ~~therefor~~ therefore not done so. Also, the results indicate that for many directions ambiguities are not relevant.

5.3 MAARSY radar

The MAARSY radar system is limited to 16 output channels but with a flexible subgroup configuration. Studies looking at interferometry of meteor echoes with MAARSY have predominantly used two different configurations. These configurations are illustrated in Figs. 4 and 5 and we hereafter refer to the them as **MAARSY-8ch** (Schult et al., 2013) and **MAARSY-15ch** (Schult et al., 2017).

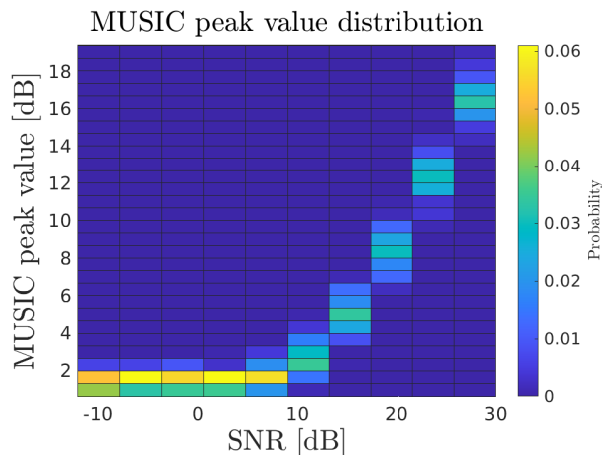


Figure 13. Distribution of MUSIC peak values as a function of SNR compiled from all MU subgroup model MC simulations with the zenith as the input DOA (cf. Fig. 11).

The phase center model of the MAARSY-8ch configuration contain many perfect ambiguities. In this antenna configuration all subgroups contain reflection-symmetry lines, which means that their individual subgroup gains do not resolve ambiguities. However, the MAARSY-8ch configuration also contains the entire array as one of the channels. This channel has a significantly different gain pattern compared to the other channels. This creates a small shift in the sensor response between different directions. We have not included an illustration of the ambiguity analysis of the phase centre model nor the subgroup model for the MAARSY-8ch configuration as they are trivial and ambiguous.

For the phase center model of the MAARSY-15ch configuration there are many close to perfect ambiguities and a few perfect ones. The distribution of ambiguities is close to identical to the MAARSY-8ch one. The addition of the smaller hexagonal subgroups, illustrated in Fig. 5, creates a decent basis for being able to determine a trajectory uniquely. But in practice, if no assumptions are applied to restrict the DOA, our results such as e.g. Fig 14 indicate that it works reliably only for high-SNR targets.

In the MAARSY-15ch configuration, half of the channels have vastly different antenna gain patterns. This fact makes the configuration better when the subgroup model is applied. We do not present any MC simulations for the phase center model of the MAARSY-15ch configuration but focus on the subgroup model.

In the MAARSY-15ch panel of Fig. 6 the sweep of worst ambiguity as a function of input DOA is illustrated. There are still a significant amount of input DOA's that produce low-distance-large inner product ambiguities using this configuration. Considering the stability inside the main lobe as indicated by the inner circle and the distribution and severity at lower elevations one can expect interferometric capabilities for a large portion of all meteor head echo events.

A significant complication was discovered regarding the application of the MUSIC algorithm on the MAARSY-15ch subgroup model: the vast differences in gain between channels narrows down the peaks in the MUSIC spectrum significantly. This is usually a desirable property as it allows more precise DOA determination. However, if the narrowing is extreme, a

simple grid search for a peak will become unreasonably costly in terms of computations. As the difference in gain between the channels increase with zenith angle, the narrowing is a function of elevation, thus making low elevation sources harder to
645 determine with grid methods.

A peak at 45° elevation from a 10 dB SNR echo would have a peak-width that requires a 3×10^5 by 3×10^5 point grid (i.e. 9×10^{10} points) to be robustly discovered, as opposed to the 200 by 200 point grid we have used for the MU radar.

As such, we applied the multiple gradient ascent method described in Sect. 3. This proved to be successful for solving the narrow-peak problem of MAARSY with a $N = 50$ and $\delta X = 0.1$ for all tested cases.

650 The most prominent problem for DOA determination of echoes in the zenith with the MAARSY-15ch configuration is that they are ambiguous with many DOAs below 57° elevation. If one can restrict the DOA to high elevations, a DOA determination algorithm should be fairly robust at correctly identifying the correct direction. This is also supported by the MC simulations of this configuration. As the results are very similar for \mathbf{k}_I , \mathbf{k}_{II} and \mathbf{k}_{III} , only the summary results for the \mathbf{k}_I simulations, without any elevation restriction, are illustrated in Fig. 14.

655 We also simulated a case where an elevation restriction was added to the DOA determination algorithm. It was found that if the algorithm could be restricted to only accept matches above 70° elevation by some reasonable arguments or using a priori data, DOA determination for \mathbf{k}_I would be stable above 15 dB SNR.

For \mathbf{k}_{III} , as illustrated in Fig. 6, the DOA determination suffers the same problem as the MU radar using the subgroup model: there are perfect ambiguities at low elevations. The general DOA determination performance is worse for the MAARSY-15ch
660 configuration than the MU radar, but they still display very similar behaviour for \mathbf{k}_{III} . The actual ~~distance-value~~ for the ambiguity is ~~$d=0.0002$~~ $d=0.9999994$, i.e. ~~22-times-smaller~~20 times closer to 1 than for the MU radar. It is unrealistic to expect this ambiguity to be resolved within any reasonable SNR for low elevation DOAs.

5.4 PANSY radar

The PANSY radar is a special and interesting case when it comes to DOA determination. Firstly, all antennas are distributed
665 vertically, ranging between -2 and +8 meters. The distribution is asymmetric also within the subgroups themselves. Secondly, as is illustrated in Fig. 4, the radar is split into 5 larger collections of subgroups. These disjoint collections are of different sizes and shapes and located relatively far apart. This radar configuration would not be analysable with conventional ambiguity analysis methods due to its complexity. These reasons also make the subgroup gain patterns even more important, a phase center approximation would be outright unphysical to consider. Thus we do not present any results for the phase center model.

670 Examining the ambiguity results for the subgroup model show very promising DOA determination capabilities. However, we can also see a potential problem with DOA determination algorithms due to the "bumpiness" of the surface. Therefore, we have applied the scattered gradient ascent method with the same configuration as for MAARSY.

The MC DOA determination simulation summary for \mathbf{k}_{II} is illustrated in Fig. 15. The results for \mathbf{k}_I and \mathbf{k}_{III} are practically identical to the results for \mathbf{k}_{II} but shifted in SNR space. Examining these summary results shows that there is no need to
675 perform the Bayesian analysis. Ambiguities are not prevalent enough and usually only one clustering forms in low SNR

MAARSY-15ch radar [Ambiguity set 1]: MC MUSIC DOA determination

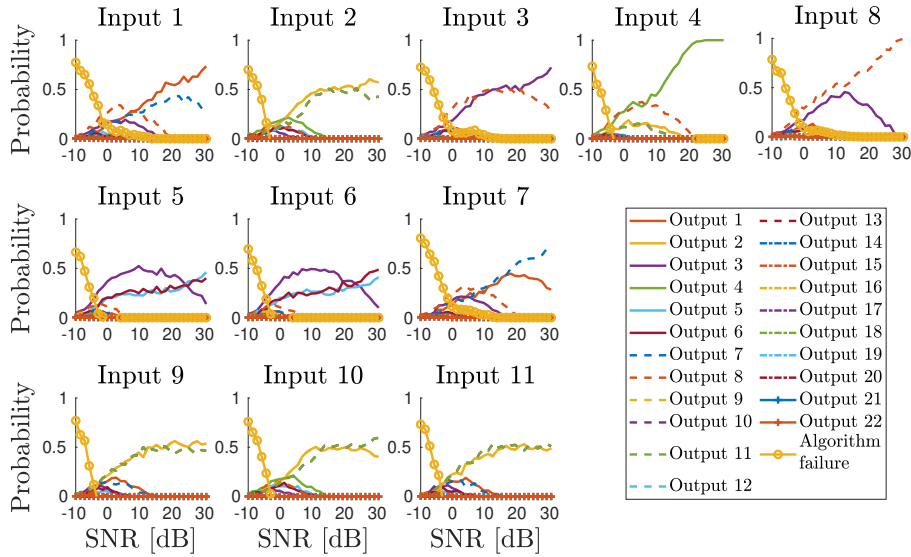


Figure 14. The discretised output DOA distribution as a function of SNR and input DOA for the MAARSY-15ch radar, using the subgroup model and \mathbf{k}_I to generate Ω_X and Ω_Y . The numerical values of Input ~~1-2-1-11~~ (Ω_X and corresponding to Output ~~1-2-1-11~~) are given in Table 1, MAARSY-15ch, I.1-~~2-11~~.

PANSY radar [Ambiguity set 2]: MC MUSIC DOA determination

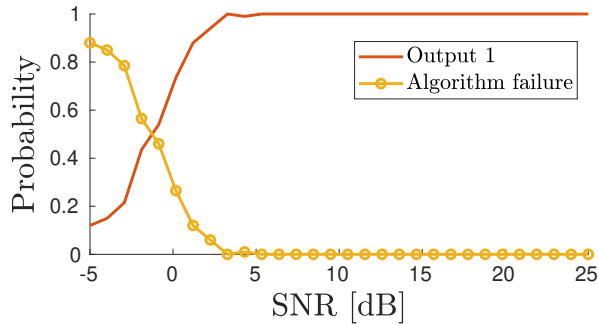


Figure 15. The discretised output DOA distribution as a function of SNR and input DOA for the PANSY radar, using the subgroup model where Input 1 is \mathbf{k}_{II} (Ω_X) and Output 1 is also \mathbf{k}_{II} (Ω_Y).

conditions. Instead of ambiguities affecting the quality of DOA determinations, sensor response model errors should be most problematic for PANSY meteor head echo observations as the system setup varies over time due to Antarctic conditions.

5.5 PANSY meteor radar

We only present summary results for the PANSY 2.5λ meteor receiver system as the very similar standard Jones 2.5λ system results have been covered in Sect. 5.1. Since the antennas are placed at the appropriate distances for a Jones 2.5λ radar in the x - y plane, but displaced in the z -direction, the actual distances between the antennas are slightly larger than a standard Jones 2.5λ system. Also, as it is not a planar array, the ambiguity situation is dependant on input DOA, as shown in Appendix B. As such it was also included in the ambiguity sweeps in Fig. 6.

To summarize the comparison between the standard Jones 2.5λ and the PANSY 2.5λ receiver: the system performs better than the standard system for DOAs originating from south-east but performs worse for the opposite direction. The MC simulations for this system is basically equivalent to the standard system, but slightly shifted in SNR space. The magnitudes of these shifts are equal to the differences of the SNR limits given in Table 1.

6 Conclusions

The main purpose of the ambiguity analysis and the MC DOA determination simulations was to provide improved understanding of DOA determination dynamics. These results and methods provide simulated theoretical references that are useful when analysing real measurement data.

We compared the phase center models and subgroup models for the MU, PANSY and MAARSY radars. For the MU radar, even though the subgroup model has ambiguities at low elevations, this is the expected behaviour in real data as well. Its performance in terms of limiting SNR is also better than the phase center model. As such, the subgroup model is overall the better choice. For the PANSY radar the situation is similar as the phase center model is outright nonphysical and should not be used. In the case of MAARSY, if the DOA search is restricted to high elevations, either model is sufficient.

The simulations also provided insight into the construction of DOA determination algorithms. It was shown for the MAARSY, MU and PANSY systems that an additional step of a scattered gradient ascent had to be implemented due to the topology of the MUSIC function. The success of this method suggests that there may be other optimization algorithms that could further improve performance, such as the Bird Swarm Algorithm (Meng et al., 2016).

The comparison between a standard Jones 2.5λ system and the PANSY meteor radar showed slight performance differences, especially in the limiting SNR as a function of input DOA. This knowledge can help calibrate thresholds for future data analysis pipelines. The comparison showed the advantage of doing ambiguity analysis and MC simulation prior to construction of such pipelines as it reveals the expected DOA determination performance of a system.

Considering the application of these methods and results on measurement data they provide a reference, not only for SNR limits, but for model validation. If measurements do not follow the dynamics simulated by these methods, assuming the pipeline itself is validated and stable, it points towards the models not representing reality. This makes such simulations a good validation tool for analysis pipelines. For example, it has been frequently shown that multiple-receiver radar systems are in need of phase calibrations (e.g. Chau et al., 2014). In the case of the results presented here: the dynamics would all be modified

710 to some degree if one would add constant phase offsets to each receiver in our models (cf. Appendix A). The framework of DOA determination simulation provides a possibility to test these matters.

We have explored a Bayesian approach to determine the most probable DOA of a target given several measurements distributed among noise-induced ambiguities. Such an approach can be applied if it is not possible to increase the SNR using coherent integration. The results indicate that this is a suitable method for providing a quantitative probability for which DOA
715 is correct. Using the Bayesian method, it appears possible to analyse echoes down to 4 dB SNR for both the standard Jones 2.5λ radar and the PANSY meteor radar, given enough independent data points from the same target.

Lastly, the MC simulations in this paper demonstrated quantitatively that ambiguities are more or less relevant depending on radar system configurations. In systems where ambiguities are not prevalent, the DOA determination failure onset is the important variable to determine. In systems where noise-induced ambiguities are relevant, it is important to determine the SNR
720 range where they emerge. Our results show that the PANSY system is not affected by noise-induced ambiguities while the MU radar has a small region of SNRs where they could be relevant. The Jones type systems and MAARSY all have relevant noise-induced ambiguities.

Table 1 contains all the MC simulations performed in our study, collected in terms of limiting SNR and input DOA. Any DOA determination on data with SNR above the limiting value will provide the correct output DOA with $> 99\%$ confidence.

725 Using interferometric radar systems to perform meteor head echo measurements, the trajectory can be directly determined (e.g. Kero et al., 2012b). Techniques like the ones presented here can be employed to avoid miss-classifying the DOA, and thereby avoiding nonphysical results. For example, the existence of high altitude radar meteors is still an open question (Gao and Mathews, 2015; Kero et al., 2019). Some previous studies have been centered on the low probability of side-lobe detections as the explanation (e.g Vierinen et al., 2014). With interferometric systems, this question could be further addressed using these
730 methods.

Data availability. All the data used in this manuscript were generated by the authors and is available in the Swedish National Data service (SND) FAIR repository at XXX.

Video supplement. An animation of the simulated MC DOA determination at different SNR for the MU radar subgroup model (with array SNR in the range from -30 dB to 10 dB) is available at the SND repository.

735 **Appendix A: Impact of known phase offsets on ambiguities**

Adding a phase offset to each element in the subgroups defined in Eq. 32 gives

$$g_j(\mathbf{k}) = \sum_{l=1}^{N_j} e^{i(\langle \mathbf{k}, \mathbf{r}_j - \boldsymbol{\rho}_{jl} \rangle_{\mathbb{R}^3} + \phi_{jl})}. \quad (\text{A1})$$

Inserting the phase offset subgroup model from Eq. A1 into Eq. 31, the explicit form of the distance-inner product calculation in Eq. 6 becomes

$$\begin{aligned} 740 \quad d(\mathbf{k})_-^2 &= \left| \sum_j^M \left(\frac{1}{|\Phi(\mathbf{k}_0)|} \sum_l^{N_j} A e^{-i(\langle \mathbf{k}_0, \boldsymbol{\rho}_{jl} \rangle + \phi_{jl})} \right) \right|^* \\ &= \left| \left(\frac{1}{|\Phi(\mathbf{k})|} \sum_l^{N_j} A e^{-i(\langle \mathbf{k}, \boldsymbol{\rho}_{jl} \rangle + \phi_{jl})} \right) \right|^2. \end{aligned} \quad (\text{A2})$$

Here * denotes complex conjugation. This form is valid for all possible phase offsets, including radars with and without subgroups. Using matrix algebra, Eq. A2 can be rewritten to

$$745 \quad d(\mathbf{k})_-^2 = \left| \frac{1}{|\Phi(\mathbf{k}_0)||\Phi(\mathbf{k})|} \sum_j^M \mathbf{w}_j^\dagger \frac{\mathbf{v}_j(\mathbf{k}_0)\mathbf{v}_j^\dagger(\mathbf{k}_0)}{|\Phi(\mathbf{k}_0)|^2} + \frac{\mathbf{v}_j(\mathbf{k})\mathbf{v}_j^\dagger(\mathbf{k})}{|\Phi(\mathbf{k})|^2} \right| = \left| \frac{\mathbf{v}_j(\mathbf{k}_0)\mathbf{v}_j^\dagger(\mathbf{k}) + \mathbf{v}_j(\mathbf{k})\mathbf{v}_j^\dagger(\mathbf{k}_0)}{|\Phi(\mathbf{k}_0)||\Phi(\mathbf{k})|} \mathbf{v}_j(\mathbf{k}_0)\mathbf{v}_j^\dagger(\mathbf{k})\mathbf{w}_j \right|, \quad (\text{A3})$$

where

$$\mathbf{w}_j = \begin{pmatrix} e^{-i\phi_{j1}} \\ \vdots \\ e^{-i\phi_{jN_j}} \end{pmatrix}, \quad \mathbf{v}_j(\mathbf{k}) = A \begin{pmatrix} e^{i\langle \mathbf{k}, \boldsymbol{\rho}_{j1} \rangle} \\ \vdots \\ e^{i\langle \mathbf{k}, \boldsymbol{\rho}_{jN_j} \rangle} \end{pmatrix}. \quad (\text{A4})$$

If $N_j = 1$, i.e. single antenna channels, then the vectors in Eq. A3 become scalars and the phase offsets \mathbf{w}_j are commutative. Thus, \mathbf{w}_j^\dagger and \mathbf{w}_j cancel to 1. As they cancel, the phase offsets do not impact $d(\mathbf{k})$. Therefore, phase offsets do not impact the ambiguity dynamics.

750 Additionally, if $\phi_{jl} = \phi_j$, i.e. phase offsets are independent of antenna in a subgroup, then $\mathbf{w}_j = e^{i\phi_j} \mathbf{1}$. The $e^{i\phi_j}$ is a scalar and is commutative. Thus, $e^{i\phi_j}$ can be moved to cancel $e^{-i\phi_j}$ and phase offsets do not impact $d(\mathbf{k})$. In all other cases, the phase offsets will affect $d(\mathbf{k})$ and change the ambiguity dynamics of a system.

The results are the same if the ambiguity indicator d is defined without the absolute value or if the the distance $|\hat{\Phi}(\mathbf{k}_0) - \hat{\Phi}(\mathbf{k})|$ is used.

755 Appendix B: Ambiguities of planar arrays with single antenna channels

What follows is a derivation of the fact that planar arrays with single antenna channels are uniquely identified by a single translated ambiguity map.

Inserting Eq. 30 into the distance-inner product calculation in Eq. 6 gives

$$\begin{aligned}
 d(\mathbf{k})^2 &= \left| \sum_j^M \frac{1}{|\Phi(\mathbf{k}_0)|} e^{-i\langle \mathbf{k}_0, \mathbf{r}_j \rangle} \frac{1}{|\Phi(\mathbf{k})|} e^{-i\langle \mathbf{k}, \mathbf{r}_j \rangle} \right|^2 = \\
 760 \quad &= \underline{2} \left(A \sum_j^M n_j \right)^{-2} \left| \sum_j^M \underline{1 - \cos(\mathbf{k} - \mathbf{k}_0, \mathbf{r}_j)} e^{-i\langle \mathbf{k} - \mathbf{k}_0, \mathbf{r}_j \rangle} \right|. \tag{B1}
 \end{aligned}$$

Eq. B1 shows that for the phase centre model, a singular function will define the morphology of the ambiguity map, only translated in \mathbf{k} space. The \mathbf{k} vectors only move on the surface of a sphere in three dimensions. When the set of \mathbf{r}_j vectors are planar, the translations become linear in two dimensions. However, if the set of \mathbf{r}_j are not planar, the projection down to two dimensions becomes non-linear and the ambiguity maps are no longer simple translations of the base function.

765 The results are the same if the ambiguity indicator d is defined without the absolute value or if the the distance $|\hat{\Phi}(\mathbf{k}_0) - \hat{\Phi}(\mathbf{k})|$ is used.

Author contributions. DK developed the model code and performed the simulations. DK prepared the manuscript with contributions from JK.

Competing interests. No competing interests are present.

770 *Acknowledgements.* We thank Koji Nishimura for providing the PANSY radar antenna configuration data, Taishi Hashimoto for providing the PANSY meteor radar antenna configuration data, and Carsten Schult for providing the MAARSY radar antenna configuration data.

References

- Bianchi, C. and Meloni, A.: Natural and man-made terrestrial electromagnetic noise: an outlook, *Annals of geophysics*, 50, 435–445, 2007.
- Campbell-Brown, M. D.: Solar cycle variation in radar meteor rates, *MNRAS*, 485, 4446–4453, <https://doi.org/10.1093/mnras/stz697>, 2019.
- 775 Ceplecha, Z., Borovička, J., Elford, W. G., Revelle, D. O., Hawkes, R. L., Porubčan, V., and Šimek, M.: Meteor Phenomena and Bodies, *Space Science Reviews*, 84, 327–471, <https://doi.org/10.1023/A:1005069928850>, 1998.
- Chau, J. L. and Clahsen, M.: Empirical Phase Calibration for Multistatic Specular Meteor Radars Using a Beamforming Approach, *Radio Science*, 54, 60–71, <https://doi.org/10.1029/2018RS006741>, 2019.
- Chau, J. L. and Woodman, R. F.: Observations of meteor-head echoes using the Jicamarca 50MHz radar in interferometer mode, *Atmospheric*
780 *Chemistry & Physics*, 4, 511–521, 2004.
- Chau, J. L., Renkowitz, T., Stober, G., and Latteck, R.: MAARSY multiple receiver phase calibration using radio sources, *Journal of Atmospheric and Solar-Terrestrial Physics*, 118, 55–63, 2014.
- Close, S., Hunt, S. M., Minardi, M. J., and McKeen, F. M.: Analysis of Perseid meteor head echo data collected using the Advanced Research Projects Agency Long-Range Tracking and Instrumentation Radar (ALTAIR), *Radio Science*, 35, 1233–1240,
785 <https://doi.org/10.1029/1999RS002277>, 2000.
- Ferreol, A., Larzabal, P., and Viberg, M.: On the asymptotic performance analysis of subspace DOA estimation in the presence of modeling errors: case of MUSIC, *IEEE Transactions on signal processing*, 54, 907–920, 2006.
- Fujiwara, Y., Kero, J., Abo, M., Szasz, C., and Nakamura, T.: MU radar head echo observations of the 2012 October Draconid outburst, *Monthly Notices of the Royal Astronomical Society*, 455, 3273–3280, 2016.
- 790 Fukao, S., Sato, T., Tsuda, T., Kato, S., Wakasugi, K., and Makihira, T.: The MU radar with active phased array system. I - Antenna and power amplifiers. II - In-house equipment, *Radio Sci.*, 20, 1155–1176, <https://doi.org/10.1029/RS020i006p01155>, 1985.
- Gao, B. and Mathews, J. D.: High-altitude radar meteors observed at Jicamarca Radio Observatory using a multibaseline interferometric technique, *MNRAS*, 452, 4252–4262, <https://doi.org/10.1093/mnras/stv1548>, 2015.
- Hashimoto, T., Saito, A., Nishimura, K., Tsutsumi, M., Sato, K., and Sato, T.: First Incoherent Scatter Measurements and Adaptive Suppression of Field-Aligned Irregularities by the PANSY Radar at Syowa Station, Antarctic, *Journal of Atmospheric and Oceanic Technology*,
795 36, 1881–1888, <https://doi.org/10.1175/JTECH-D-18-0175.1>, 2019.
- Hassenpflug, G., Yamamoto, M., Luce, H., and Fukao, S.: Description and demonstration of the new Middle and Upper atmosphere Radar imaging system: 1-D, 2-D, and 3-D imaging of troposphere and stratosphere, *Radio Sci.*, 43, RS2013,
<https://doi.org/10.1029/2006RS003603>, 2008.
- 800 Hocking, W. K.: A new approach to momentum flux determinations using SKiYMET meteor radars, *Ann. Geophys.*, 23, 2433–2439, <https://doi.org/10.5194/angeo-23-2433-2005>, <https://www.ann-geophys.net/23/2433/2005/>, 2005.
- Hocking, W. K., Fuller, B., and Vandeeper, B.: Real-time determination of meteor-related parameters utilizing modern digital technology, *Journal of Atmospheric and Solar-Terrestrial Physics*, 63, 155–169, [https://doi.org/10.1016/S1364-6826\(00\)00138-3](https://doi.org/10.1016/S1364-6826(00)00138-3), 2001.
- Holdsworth, D. A.: Angle of arrival estimation for all-sky interferometric meteor radar systems, *Radio Sci.*, 40, RS6010,
805 <https://doi.org/10.1029/2005RS003245>, 2005.
- Jones, J., Webster, A. R., and Hocking, W. K.: An improved interferometer design for use with meteor radars, *Radio Science*, 33, 55–65, <https://doi.org/10.1029/97RS03050>, 1998.

- Jones, J., Brown, P., Ellis, K. J., Webster, A. R., Campbell-Brown, M., Krzemenski, Z., and Weryk, R. J.: The Canadian Meteor Orbit Radar: system overview and preliminary results, *Planetary and Space Science*, 53, 413–421, <https://doi.org/10.1016/j.pss.2004.11.002>, 2005.
- 810 Kangas, A., Stoica, P., and Soderstrom, T.: Finite sample and modelling error effects on ESPRIT and MUSIC direction estimators, *IEE Proceedings-Radar, Sonar and Navigation*, 141, 249–255, 1994.
- Kangas, A., Stoica, P., and Söderström, T.: Large-sample analysis of MUSIC and Min-Norm direction estimators in the presence of model errors, *Circuits, Systems and Signal Processing*, 15, 377–393, 1996.
- Kastinen, D.: Determining all ambiguities in direction of arrival measured by radar systems, *Radio Sci Bull*, 333, 3À33, 2018.
- 815 Kastinen, D. and Kero, J.: A Monte Carlo-type simulation toolbox for Solar System small body dynamics: Application to the October Draconids, *Planetary and Space Science*, 143, 53–66, <https://doi.org/10.1016/j.pss.2017.03.007>, 2017.
- Kero, J., C., S., T., N., T., T., H., M., and K., N.: First results from the 2009–2010 MU radar head echo observation programme for sporadic and shower meteors: the Orionids 2009, *Monthly Notices of the Royal Astronomical Society*, 416: 2550–2559. doi: 10.1111/j.1365-2966.2011.19146.x, 2011.
- 820 Kero, J., C., S., T., N., D., M. D., M., U., Y., F., T., T., H., M., and K., N.: The 2009–2010 MU radar head echo observation programme for sporadic and shower meteors: radiant densities and diurnal rates., *Monthly Notices of the Royal Astronomical Society*, 425: 135–146. doi: 10.1111/j.1365-2966.2012.21407.x, 2012a.
- Kero, J., C., S., T., N., T., T., H., M., and K., N.: A meteor head echo analysis algorithm for the lower VHF band, *Ann. Geophys.*, 30, 639., 2012b.
- 825 Kero, J., Szasz, C., and Nakamura, T.: MU head echo observations of the 2010 Geminids: radiant, orbit, and meteor flux observing biases, *Ann. Geophys.*, 31, 439–449, <https://doi.org/10.5194/angeo-31-439-2013>, <http://www.ann-geophys.net/31/439/2013/>, 2013.
- Kero, J., Campbell-Brown, M. D., Stober, G., Chau, J. L., Mathews, J. D., and Pellinen-Wannberg, A.: Radar Observations of Meteors, p. 65, 2019.
- Kildal, P.-S.: Foundations of antenna engineering: a unified approach for line-of-sight and multipath, chap. Terminology, quantities, units and symbols, pp. 7–11, Kildal Antenn AB, Gothenburg, Sweden, 2015.
- 830 Latteck, R., Singer, W., Rapp, M., and Renkwitz, T.: MAARSY - the new MST radar on Andøya/Norway, *Adv. Radio Sci.*, 8, 219–224, <https://doi.org/10.5194/ars-8-219-2010>, 2010.
- McCrea, I., Aikio, A., Alfonsi, L., Belova, E., Buchert, S., Clilverd, M., Engler, N., Gustavsson, B., Heinselman, C., Kero, J., Kosch, M., Lamy, H., Leyser, T., Ogawa, Y., Oksavik, K., Pellinen-Wannberg, A., Pitout, F., Rapp, M., Stanislawska, I., and Vierinen, J.: The science case for the EISCAT_3D radar, *Progress in Earth and Planetary Science*, 2, 21, <https://doi.org/10.1186/s40645-015-0051-8>, 2015.
- 835 Meng, X.-B., Gao, X. Z., Lu, L., Liu, Y., and Zhang, H.: A new bio-inspired optimisation algorithm: Bird Swarm Algorithm, *Journal of Experimental & Theoretical Artificial Intelligence*, 28, 673–687, 2016.
- Nishimura, K., Sato, T., Nakamura, T., and Ueda, M.: High sensitivity radar-optical observations of faint meteors, *IEICE Trans. Comm.*, E84-C, 1877–1884, 2001.
- 840 Polensky, E.: LFmap: A low frequency sky map generating program, *Long Wavelength Array Memo Series*, 111, 2007.
- Renkwitz, T., Singer, W., Latteck, R., Stober, G., and Rapp, M.: Validation of the radiation pattern of the Middle Atmosphere Alomar Radar System (MAARSY), *Adv. Radio Sci.*, 10, 245–253, <https://doi.org/10.5194/ars-10-245-2012>, 2012.
- Renkwitz, T., Stober, G., Latteck, R., Singer, W., and Rapp, M.: New experiments to validate the radiation pattern of the Middle Atmosphere Alomar Radar System (MAARSY), *Adv. Radio Sci.*, 11, 283–289, <https://doi.org/10.5194/ars-11-283-2013>, 2013.

- 845 Renkwitz, T., Schult, C., Latteck, R., and Stober, G.: Validation of the radiation pattern of the VHF MST radar MAARSY by scattering off a sounding rocket's payload, *Adv. Radio Sci.*, 13, 41–48, <https://doi.org/10.5194/ars-13-41-2015>, 2015.
- Renkwitz, T., Schult, C., and Latteck, R.: VHF antenna pattern characterization by the observation of meteor head echoes, *Atmos. Meas. Tech.*, 10, 527–535, <https://doi.org/10.5194/amt-10-527-2017>, 2017.
- Sato, K., Tsutsumi, M., Sato, T., Nakamura, T., Saito, A., Tomikawa, Y., Nishimura, K., Kohma, M., Yamagishi, H., and Yamanouchi, T.: Program of the Antarctic Syowa MST/IS radar (PANSY), *Journal of Atmospheric and Solar-Terrestrial Physics*, 118, 2–15, <https://doi.org/10.1016/j.jastp.2013.08.022>, 2014.
- 850 Schmidt, R. O.: Multiple emitter location and signal parameter estimation, *IEEE Transactions on Antennas and Propagation*, 34, 276–280, <https://doi.org/10.1109/TAP.1986.1143830>, 1986.
- Schult, C., Stober, G., Chau, J. L., and Latteck, R.: Determination of meteor-head echo trajectories using the interferometric capabilities of MAARSY, *Annales Geophysicae*, 31, 1843–1851, <https://doi.org/10.5194/angeo-31-1843-2013>, 2013.
- 855 Schult, C., Stober, G., Janches, D., and Chau, J. L.: Results of the first continuous meteor head echo survey at polar latitudes, *Icarus*, 297, 1–13, <https://doi.org/10.1016/j.icarus.2017.06.019>, 2017.
- Szasz, C., Kero, J., Meisel, D. D., Pellinen-Wannberg, A., Wannberg, G., and Westman, A.: Orbit characteristics of the tristatic EISCAT UHF meteors, *Monthly Notices of the Royal Astronomical*, 388, 15–25, <https://doi.org/10.1111/j.1365-2966.2008.13374.x>, 2008.
- 860 Vaubaillon, J., Colas, F., and Jorda, L.: A new method to predict meteor showers. I. Description of the model, *Astronomy and Astrophysics*, 439, 751–760, <https://doi.org/10.1051/0004-6361:20041544>, 2005a.
- Vaubailon, J., Colas, F., and Jorda, L.: A new method to predict meteor showers. II. Application to the Leonids, *Astronomy and Astrophysics*, 439, 761–770, <https://doi.org/10.1051/0004-6361:20042626>, 2005b.
- Vierinen, J., Fentzke, J., and Miller, E.: An explanation for observations of apparently high-altitude meteors, *MNRAS*, 438, 2406–2412, <https://doi.org/10.1093/mnras/stt2358>, 2014.
- 865 Whipple, F. L.: A Comet Model. II. Physical Relations for Comets and Meteors., *The Astrophysical Journal*, 113, 464, <https://doi.org/10.1086/145416>, 1951.
- Younger, J. P. and Reid, I. M.: Interferometer angle-of-arrival determination using precalculated phases, *Radio Sci.*, 52, 1058–1066, <https://doi.org/10.1002/2017RS006284>, 2017.

Table 1. Summary results for all input DOAs used to perform an MC DOA determination simulation. These are the Ω_X sets for $\mathbf{k}_I, \mathbf{k}_{II}$ and \mathbf{k}_{III} . These limits show when the DOA determination with MUSIC for the respective radar system is stable to a level of 99% output probability of the true input. Thus for the given DOA, echoes below the given SNR are possible ambiguous. In the column header Az stands for Azimuth angle and El for Elevation angle in local radar coordinates. An empty SNR indicates that none of the simulations produced an Input-Output correspondence of 99% or higher. For the MU, MAARSY and PANSY radars these results are using the model described by Eq. 31. For the Jones 2.5 λ and the PANSY 2.5 λ the model in Eq. 30 was used. The ~~index corresponds~~ indices correspond to the initial \mathbf{k} vector and the Input-Output maps illustrated for each radar system in Sect. 5.

Index	Az [°]	El [°]	SNR [dB]	Index	Az [°]	El [°]	SNR [dB]	Index	Az [°]
Jones 2.5 λ				MU				PA	
I.1	-60.25 -60.63	59.70-59.60	8.97-15.86	I.1	26.70-87.15	30.28-72.13	3.10-1.03	I.1	-60.70 -33.55
I.2	60.24-113.52	59.70-61.08	15.86-8.97	I.2	135.84-169.72	35.16-58.77	5.86-6.55	I.2	179.89-60.66
I.3	0-179.33	46.50-79.01	17.59-12.41	I.3	-16.93-126.53	27.81-60.68	-0.34	I.3	-0.50-113.94
I.4	0-0.18	75.50-46.26	12.41-17.59	I.4	-146.41-3.72	37.47-52.37	-2.41	I.4	0-179.26
I.5	180-144.89	79.18-39.22	12.41	I.5	87.16-146.41	72.13-37.47	-1.03-	I.5	60.27-0.00
H.1 I.6	180-60.20	64.02-59.46	23.97-8.97	I.6	0-26.70	75.50-30.27	1.72-	I.6	-33.53-0.51
H.2 I.7	0-152.76	90-13.23	23.97-19.31	I.7	-161.89-33.30	81.10-56.18	1.72-5.17	I.7	-152.88-103.93
H.3 I.8	90-0.00	64.02-75.50	23.97-14.14	H.1 I.8	0-0.00	90-75.50	16.67-1.03	I.8	60.88
I.9	32.58	34.58	14.14	I.9	144.19	63.80	-2.41	I.9	145.82
I.10	-102.45	25.12	12.41	I.10	109.76	49.88	-6.55	II.1	90.44-32.97
II.4.1	-90-135.00	64.03-51.17	23.97	III.1 I.11	-162.24-41.21	20.67-58.17	35.59-0.34	II.2	-65.37-90.28
II.5.2	0-116.75	64.02-8.09	22.07-27.76	III.2 II.1	145.18-27.64	43.81-90.00	39.66-16.67	II.3	-0.33-90.85
III.1 II.3	10.84-89.71	56.53-63.84	12.41-23.97	III.3.1	45-45.00	40-40.00	34.24	II.4	-90.46-179.94
III.2 II.4	79.16-179.72	56.53-63.83	12.41-22.07	III.4.2	17.27-26.28	38.06-20.42	36.95-38.31	II.5	-28.23-0.51
III.3 II.5	45-103.35	40-90.00	12.41-23.97	III.5.3	-26.29-145.18	20.41-43.81	38.31-39.66	II.6	-45.84-28.23
II.6	45.00	51.17	23.97	III.6.4	-138.92-162.23	25.43-20.66	36.95-34.24	II.7	-179.67-45.83
I.1 II.7	-139.11-63.25	67.37-8.08	23.10-27.76	PANSY				II.8	0-65.41
I.2 II.8	0-0.28	75.50-63.84	30-23.97	II.1	0-98.84	90-90.00	3.28	II.9	119.07
II.9	26.75	8.09	27.76	MAARSY-15ch				II.10	135.85
II.10	-90.29	63.83	23.97	I.1	-71.17	49.50	-	III.1	-11.52-45.00
II.1 11	0-153.25	90-8.09	-27.76	I.2	173.42	35.64	-	III.2	78.53-120.83
III.1	45-74.33	40-69.17	-14.14	I.3	64.25	47.34	-	III.3	5.55-78.60
III.2	-135-79.43	31.62-56.71	-12.41	I.4	-139.15	67.37	24.48	III.4	45-169.87
III.3	164.33	69.17	14.14	I.5	-111.75	19.13	-	III.5	-79.52
III.4	45.00	40.00	12.41	I.6	18.55	33.16	-	III.6	85.27
III.5	44.98	82.01	14.14	I.7	102.44	13.94	-	III.7	5.50
III.6	-135.00	36.11	7.24	I.8	0.01	75.50	30.00	III.8	10.80
III.7	10.57	56.72	14.14	I.9	175.81	35.15	-	III.9	-148.83
H.1 III.8	0-135.00	90-60.76	15-12.41	I.10	-23.32	34.67	-		